nature energy

ARTICLES

https://doi.org/10.1038/s41560-019-0508-x

Gradient Li-rich oxide cathode particles immunized against oxygen release by a molten salt treatment

Zhi Zhu[1], Daiwei Yu[2], Yang Yang[1], Cong Su[1], Yimeng Huang[1], Yanhao Dong[1], Iradwikanari Waluyo[3], Baoming Wang[4], Adrian Hunt[3], Xiahui Yao[1], Jinhyuk Lee[1], Weijiang Xue[1] and Ju Li[1*]

Lithium-rich transition metal oxide ($Li_{1+X}M_{1-X}O_2$) cathodes have high energy density above 900 Wh kg^{-1} due to hybrid anion- and cation-redox (HACR) contributions, but critical issues such as oxygen release and voltage decay during cycling have prevented their application for years. Here we show that a molten molybdate-assisted LiO extraction at 700 °C creates lattice-coherent but depth (r)-dependent $Li_{1+X(r)}M_{1-X(r)}O_2$ particles with a Li-rich ($X \approx 0.2$) interior, a Li-poor ($X \approx -0.05$) surface and a continuous gradient in between. The gradient Li-rich single crystals eliminate the oxygen release to the electrolyte and, importantly, still allow stable oxygen redox contributions within. Both the metal valence states and the crystal structure are well maintained during cycling. The gradient HACR cathode displays a specific density of 843 Wh kg^{-1} after 200 cycles at 0.2C and 808 Wh kg^{-1} after 100 cycles at 1C, with very little oxygen release and consumption of electrolyte. This high-temperature immunization treatment can be generalized to leach other elements to avoid unexpected surface reactions in batteries.

As the energy density ceiling (~700 Wh kg^{-1}) of conventional lithium transition metal oxide ($LiMO_2$, M = Ni, Co, Mn) cathodes is approached, hybrid anion- and cation-redox (HACR) cathodes[1] compete with purely anion-redox Li_nS and Li_nO (refs. [2,3]) cathodes as candidates for next-generation batteries. Li-rich $Li_{1+X}M_{1-X}O_2$ (LXMO) with a layered structure is one of the most promising HACR cathodes[4,5]. The lattice structure is a solid solution or a fine-phase mixture of Li_2MnO_3 and $LiMn_aNi_bCo_{1-a-b}O_2$ (NMC) lattice motifs[6,7], with Li-layer (LiL) and transition metal-layer (TML) cation sites. In the Li_2MnO_3 motif, one-third of Mn ions in the TML are replaced by Li ions (Li_{TML}), leading to plenty of axial Li–O–Li configurations (each O is bonded to six Li/M)[8]. Consequently, certain O_{2p} orbitals are less hybridized with the transition metal (M) d orbitals, and thus they have higher energies than those in 100% axial Li–O–M configurations[9] (as in NMC). These oxygen anions in LXMO could be oxidized more easily when the material is charged and subsequently contribute to capacity in battery cycles.

Anion-redox capacity can be reversible or irreversible. To harness the oxygen anion-redox contribution to double the energy density, it behoves one to ponder the cause of irreversibility. It has been reported[10,11] that the migration barrier of O^- is only 0.9 eV, whereas that of O^{2-} is 2.3–4.0 eV in Li_2MnO_3. Generally, the oxidation of $O^{2-} \rightarrow O^{\alpha-}$ ($\alpha < 2$, peroxide- or superoxide-like)[12] when charged to high voltages (>4.3 V versus Li^+/Li) makes oxygen more mobile and easier to escape from a metal oxide particle, resulting in oxygen vacancies, transition metal co-migration and structural collapse, with a telltale fingerprint of continuous voltage decay[10,13–16] and consumption of electrolyte[17]. Oxygen release into the liquid electrolyte must be prevented in battery cycling.

In uniformly Li-rich particles, structural collapse tends to start from the surface[11,18,19]. Wang et al.[10] reported that once O vacancies are produced at the surface of LXMO, a massive number of new structural flaws nucleate, leading to the propagation of the crystal collapse into the whole particle. The oxygen release will persist over hundreds of cycles, with continuous M reduction and oxygen void formation[10,15,16]. While metal oxide coatings[20,21] and other surface treatments[22] were performed to improve the cycling capacity, few have addressed the problem of voltage fading and electrolyte consumption.

Inside LXMO, the heavy use of O redox triggers local oxygen mobility. But global oxygen mobility, defined by percolating oxygen transport from the particle core to the surface, should be avoided at all costs. As shown in Fig. 1a, if near the surface, we can remove all Li_{TML} and even substitute some Li_{LiL} with M_{LiL} without disrupting the single crystallinity, then the M valence can be locally reduced, which would ensure less anion redox in cycling (Supplementary Fig. 1). When we make $X < 0$ near the surface ('Li poor'), the initial M valence would drop below +3, which suppresses anion redox while promoting cation redox, which will lower the concentration of mobile $O^{\alpha-}$ ($\alpha < 2$) near the surface.

Herein we demonstrate a concept of full Li-gradient $Li_{1+X(r)}M_{1-X(r)}O_2$ ($LX_{(r)}MO$) particles, as illustrated in Fig. 1b, where $X(r)$ is a function of position r, with $X(r_{core}) = X_{rich} > 0$, where r_{core} is the interior of the particle ($X_{rich} = 0.2$ in this work) and $X(r_{surface}) = X_{poor} \leq 0$. In other words, we make $X_{poor} < 0$ to cut down both O anion redox and mobility near the surface without extra lattice defects[23]. The gradient design calls for the primary particles to be crystallographically coherent from the Li-rich bulk to the Li-poor surface (Fig. 1c–e), instead of having grain or phase boundaries in between like traditional coatings.

---

[1]Department of Nuclear Science and Engineering and Department of Materials Science and Engineering, Massachusetts Institute of Technology, Cambridge, MA, USA. [2]Department of Electrical Engineering and Computer Science, Massachusetts Institute of Technology, Cambridge, MA, USA. [3]National Synchrotron Light Source II, Brookhaven National Laboratory, Upton, NY, USA. [4]Materials Research Laboratory, Massachusetts Institute of Technology, Cambridge, MA, USA. *e-mail: liju@mit.edu

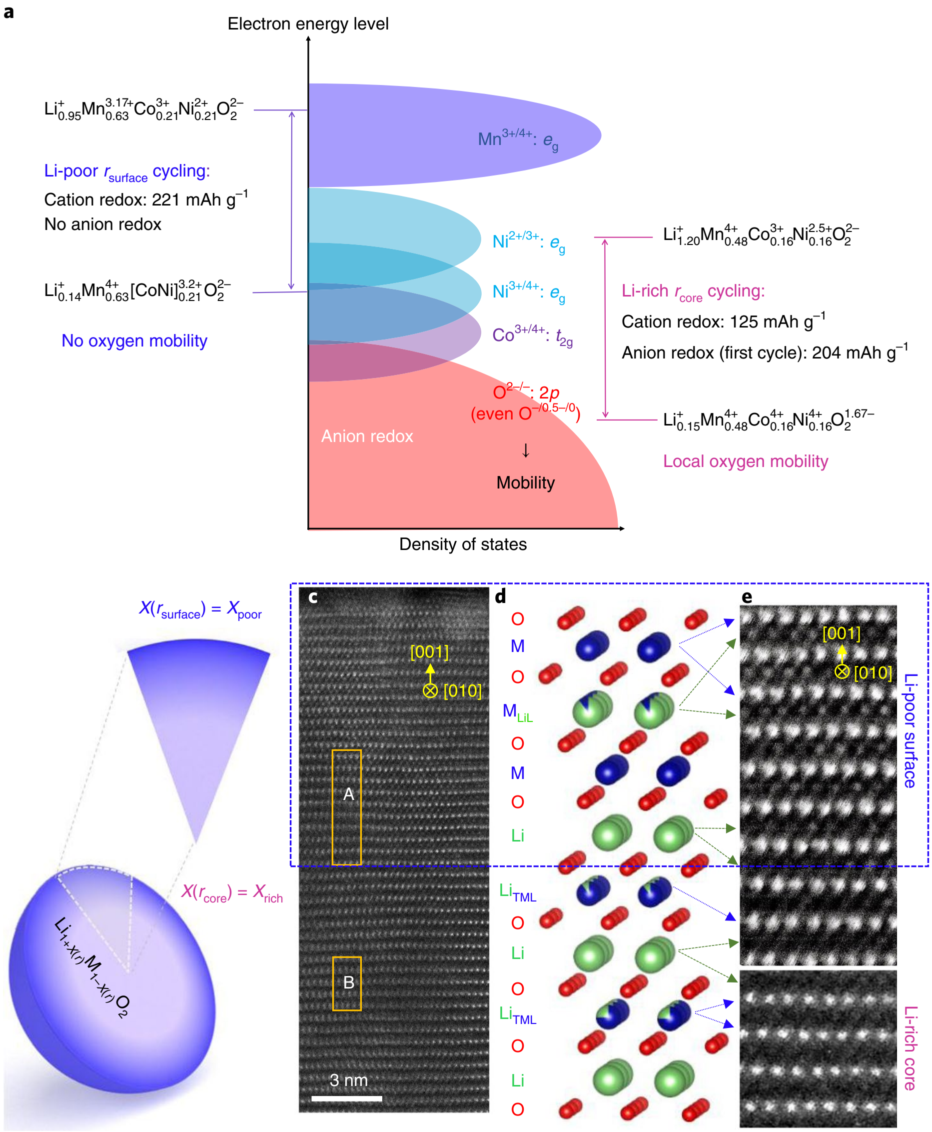

Fig. 1 | Redox behaviour and structural design of $Li_{1+X(r)}M_{1-X(r)}O_2$ particles with a continuous gradient from the Li-rich bulk to the Li-poor surface. **a**, Redox behaviours of transition metal cations and oxygen anions of the Li-poor surface and the Li-rich bulk. **b**, Schematic of the cross-section of a $Li_{1+X(r)}M_{1-X(r)}O_2$ particle. The zoomed-in sector is a two-dimensional cross-section from the particle bulk to the surface. The deeper colour indicates more M and less Li. **c**, STEM-HAADF lattice image from the core to the surface in a lattice-coherent particle. Rectangle A is from the Li-poor surface, and rectangle B is from the Li-rich bulk. The circle with the cross inside denotes the direction travelling into the page. **d**, Schematic of the layered structure of the Li-gradient region in a lattice-coherent particle from the Li-rich (Li substitution in M layer) bulk to the Li-poor (M substitution in Li layer) surface. **e**, STEM-HAADF images from rectangle A and rectangle B in **c** with higher magnification, where M_{LiL} pillars can clearly be seen in the Li layers (due to higher average atomic number, *Z*, of the atomic column) in rectangle A but not in B.

This continuous gradient from 'Li richness' to 'Li poorness' in the $LX_{(r)}MO$ single crystal achieves the following goals. First, the Li-rich core ($Li_{1.2}M_{0.8}O_2$) that takes up most of the particle volume has very high capacity, due to oxygen anion-redox contribution from the ample axial Li–O_{2p}–Li configurations[9] (region B in Fig. 1c) embedded inside, akin to the Li_2O–LiO–LiO_2 'solid oxygen cathode' concept[2] but well mixed at the atomic scale. Meanwhile, the epitaxially coherent Li-poor region near the surface (region A in Fig. 1c), which mainly features Li–O–M and even M–O–M configurations, prevents oxygen ions from being oxidized and escaping into the electrolyte. The M_{LiL} pillars would greatly stabilize the layered structure[4] (Fig. 1d,e) at the surface. Essentially, the Li-poor surface can be considered 'immunized' against oxygen release in electrochemical cycling, due to earlier preventive ejections of LiO from the surface at a high annealing temperature of 700 °C. Then the oxygen redox in room-temperature cycling can only happen in the bulk, but oxygen cannot trespass the 'immunized' Li-poor surface and escape into the electrolyte. Second, in practical full cells, very little liquid electrolyte is used. Since the carbonate electrolyte can be oxidized easily in the presence of freed oxygen[24–26], minimizing oxygen release ensures a long battery life under parsimonious electrolyte condition. In subsequent sections, we will demonstrate excellent voltage retention of our $LX_{(r)}MO$ material against $Li_4Ti_5O_{12}$ anode in capacity-matched full cells with parsimonious electrolyte (2 g Ah^{-1}) and at relatively high C-rates ≥1C (1C ≡ 250 mA g^{-1}).

Creation of Li-gradient single crystals

Pioneering work has been done to create gradient distribution in transition metals Ni, Mn and Co[27,28]. However, there have been no attempts to create gradients in Li richness/poorness (Li_{TML}/M_{LiL}) as it appears that Li^+ ions can easily diffuse throughout the particle, making it challenging to maintain a Li gradient in primary particles. But scrutiny of the $Li_{1+X(r)}M_{1-X(r)}O_2$ concept indicates that a Li gradient in an uncharged state is equal and opposite to a M gradient. M would be a slow diffuser if there were no M vacancies or other lattice defects, so this 'Li gradient' in the discharged state could stay a permanent feature at room temperature. Constructing this M gradient requires a high-temperature process, so in this work we develop a high-temperature leaching method with molten MoO_3. We start with uniform-concentration Li-rich LXMO particles, which react with a small amount of sintering aid (liquid molybdate) at 700 °C via the following reaction:

$$\begin{aligned}&Li_{1+X_{rich}}M_{1-X_{rich}}O_2+\beta MoO_3 \quad \rightarrow\\&Li_{1+X_{rich}-2\beta}M_{1-X_{rich}}O_{2-2\beta}+\beta Li_2MoO_4+\tfrac{\beta}{2}O_2(\uparrow)\end{aligned} \tag{1}$$

in effect extracting $2\beta LiO=\beta Li_2O+\frac{\beta}{2}O_2(\uparrow)$from the near-surface region of LXMO, where β is the progress variable. The sintering aid works by reacting with the ceramic host to form a liquid layer (MoO_3-Li_2O eutectic liquid solution at >525 °C, Supplementary Fig. 2), wetting and wrapping around the host particles. The temperature is also high enough to anneal the layered crystal, eliminating Li/O vacancies left behind to obtain a dense crystal[29]:

$$\begin{aligned}&Li_{1+X_{rich}-2\beta}M_{1-X_{rich}}O_{2-2\beta} \quad \rightarrow\\&(1-\beta)Li_{(1+X_{rich}-2\beta)/(1-\beta)}M_{(1-X_{rich})/(1-\beta)}O_2\\&\equiv(1-\beta)Li_{1+X_{poor}}M_{1-X_{poor}}O_2\end{aligned} \tag{2}$$

with $X_{poor}=(X_{rich}-\beta)/(1-\beta)$ and some volume shrinkage.

Liquid-phase diffusion is much more rapid than solid-state diffusion, so reaction (1) is initially rate-controlled by solid-state diffusion. Thus the progress variable β in $Li_{1+X_{rich}-2\beta}M_{1-X_{rich}}O_{2-2\beta}$ is spatially dependent, with $\beta(r_{core})\approx 0$, while $\beta(r_{surface})>0$ or even as large as $\beta(r_{surface})>X_{rich}$. In other words, the surface can actually become Li poor while the core still keeps the initial Li richness. As long as the MoO_3 fraction, w, is small (such as 4–6 wt%), the liquid will reach thermodynamic saturation at time $t_{saturation}$ for dissolving Li_2O, after which no more LiO can be leached out. By adjusting w and duration t of reaction (1), we are able to throttle $\beta(r_{surface})\geq X_{rich}$ and end up with $X_{poor}=(X_{rich}-\beta)/(1-\beta)\leq 0$ on the surface, while still keeping an X_{rich} core.

Reactions (1) and (2) require only basic solid-state reaction in an air furnace and are highly scalable. Because Li_2MoO_4 is water soluble, a simple sonication in water can etch away the Li_2MoO_4 at room temperature by

$$Li_2MoO_4\rightarrow 2Li^+(aq)+MoO_4^{2-}(aq) \tag{3}$$

With reactions (1)–(3), we created a Li-gradient region at the surface of, originally, $Li_{1.20}Mn_{0.48}Co_{0.16}Ni_{0.16}O_2$ (labelled as G_0) particles with 4 wt% MoO_3 leaching ($G_0\rightarrow G_4$) and obtained the lattice-coherent $LX_{(r)}MO$ particles. As we can see from the X-ray diffraction (XRD) pattern and STEM high-angle annular dark field (HAADF) in Supplementary Fig. 3, G_0 featured a conventional Li-rich layered structure[6,7]. As expected, the new phase that appeared after reactions (1) and (2) had the composition of Li_2MoO_4 (Supplementary Fig. 4) instead of MoO_3. The scanning transmission electron microscopy energy-dispersive X-ray spectroscopy (STEM-EDS) mapping in Fig. 2a showed that the newly formed Li_2MoO_4 was located only at the particle surface. The XRD pattern and EDS mapping on G_4 (Supplementary Fig. 5) confirmed that Li_2MoO_4 was completely removed after sonication in water, while no Mn, Co or Ni was lost from the particle (Supplementary Table 1). The XRD pattern also indicated that the structure of the final product (G_4) after reactions (1)–(3) remained unchanged compared with G_0. The inductively coupled plasma atomic emission spectroscopy (ICP-AES) analysis in Fig. 2b and Supplementary Table 2 showed that the particle-averaged Li content decreased from 1.221 ± 0.003 (G_0) to 1.173 ± 0.003 (G_4) (± s.d.). The well-retained layered structure and epitaxial crystallinity from the bulk up to the surface in G_4 can be visualized by the STEM-HAADF image in Fig. 1c and the high-resolution transmission electron microscopy (HRTEM) image in Supplementary Fig. 3.

An electron energy-loss spectroscopy (EELS) line scan was used to quantify the Li-gradient profile across the G_4 particle (diameter ≈ 400 nm), as shown in Fig. 2c. Since Li can barely be quantified by EELS, we sum up the molar ratio of transition metal to oxygen, $\sigma\equiv M/O=\sum(Mn+Co+Ni)/O$, which should be equal to $(1-X(r))/2$ for $Li_{1+X(r)}M_{1-X(r)}O_2$, to obtain the $X(r)$ profile. As shown in Fig. 2d, the $X\approx 0.20$ in the bulk agreed well with the feedstock $Li_{1.20}Mn_{0.48}Co_{0.16}Ni_{0.16}O_2$, but near the surface, within a depletion zone thickness of ~17 nm, $X(r)$ gradually decreased from 0.20 to about −0.05 from the bulk to the surface (the ratio of Mn, Co and Ni was kept close to 3:1:1 everywhere). Thus, the Li-poor surface had a composition of $Li_{0.95}Mn_{0.63}Co_{0.21}Ni_{0.21}O_2$. The $X(r)$ profile of the particles leached with 6 wt% MoO_3 (G_6) is shown in Supplementary Fig. 6, which indicates an ~18 nm Li-depletion region from $Li_{1.20}Mn_{0.48}Co_{0.16}Ni_{0.16}O_2$ to ~$Li_{0.90}Mn_{0.66}Co_{0.22}Ni_{0.22}O_2$ at the surface of an ~310 nm particle. The thickness and depletion extent of this Li-gradient layer can be adjusted based on the amount of MoO_3 (Supplementary Discussion 1 and Supplementary Table 3), the leaching temperature and the time to optimize the electrochemical performance.

The composition gradient resulted in a decreased XRD intensity ratio of $I(003)/I(104)$ (Supplementary Fig. 3) due to M_{LiL} in G_4 (Fig. 2e). It has been reported that small amounts of M_{LiL} pillars can stabilize the layered structure in cycling[4,30]. The Li-gradient region also has reduced cation valence, as LiO was leached from the particle to keep charge balance from $Li^+_{1.20}Mn^{4+}_{0.48}Co^{3+}_{0.16}Ni^{2.5+}_{0.16}O_2^{2-}(r_{core})$ to $Li^+_{0.95}Mn^{3.17+}_{0.63}Co^{3+}_{0.21}Ni^{2+}_{0.21}O_2^{2-}(r_{surface})$. The increased ratio of Mn L_3 peak area to L_2 peak area (A_{L3}/A_{L2}) on the EELS curve in Fig. 2f clearly indicates that Mn^{3+} was generated[31,32] and gradually increased in concentration from the bulk to the surface. There is electrostatic potential variation and band bending inside the particles, similar to p–n junction with gradient doping. The reduced valences of other M from the Li-rich bulk to the Li-poor surface were shown with soft X-ray absorption spectroscopy (sXAS) in Supplementary Fig. 7. Pre-positioning these reduced-valence M_{LiL} at the surface suppresses anion redox and keeps the surface fully dense in cycling.

Therefore, we have successfully synthesized $LX_{(r)}MO$ single crystals with fully coherent layered lattice even when Li content varied from very rich ($X=0.2$) to slightly poor ($X=-0.05$). All the oxygen sites in $Li_{1+X(r)}M_{1-X(r)}O_2$ were fully occupied and formed an integral oxygen framework, favourable for both Li and electron conduction[33], as well as stress accommodation[27]. This is substantially different from coatings, which have unavoidable grain or phase boundaries that are preferential locations for stress-induced spallation and oxygen mobility.

Suppressed oxygen release and enhanced cycling of $LX_{(r)}MO$

Differential electrochemical mass spectrometry (DEMS) was performed on G_0, G_4 and G_6 samples. From Fig. 3a, an O_2 (gas) evolution peak of 3.4×10^{-4} μmol was detected from G_0 in the first cycle, but very little O_2 (gas) was detected from either G_4 or G_6. In the second cycle, the O_2 (gas) signals for G_4 and G_6 were entirely absent, while there was still an obvious O_2 (gas) signal for G_0. Thus, the Li-gradient surface had indeed suppressed oxygen gas release in charging. Also, a notable amount of CO_2 (gas) was released from G_0, which was almost absent for G_4 or G_6. This is the key evidence for carbonate electrolyte

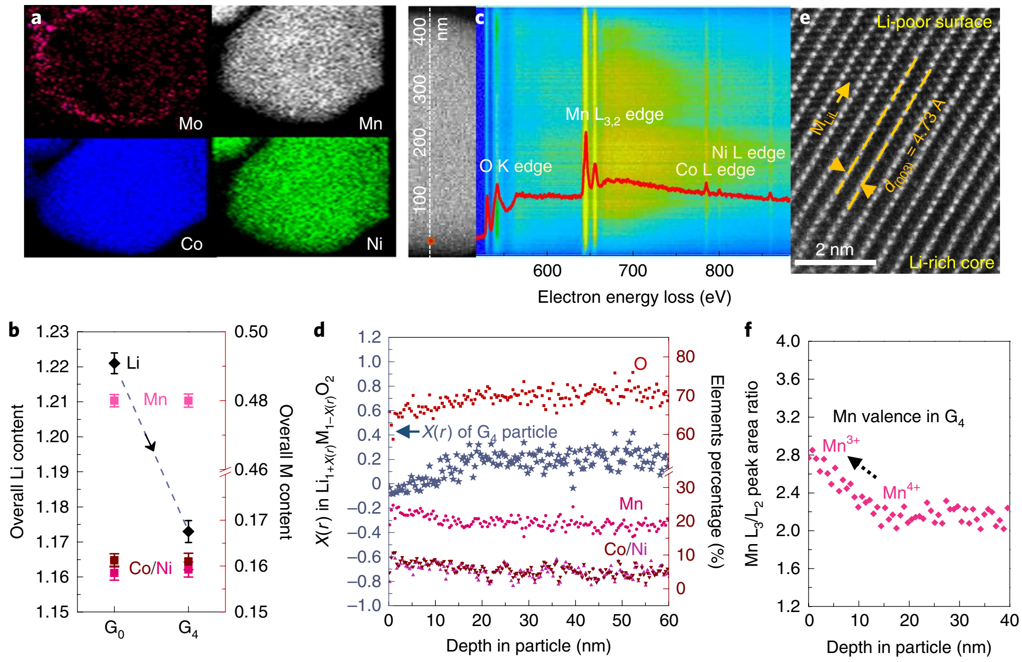

Fig. 2 | Characterizations of $Li_{1+X(r)}M_{1-X(r)}O_2$ single crystals and quantification of $X(r)$. **a**, STEM-EDS mapping of the particle after reactions (1) and (2), indicating that Mo was concentrated at the particle surface, while Mn, Co and Ni were located everywhere. **b**, Average Li (black, left *y*-axis) and M (other colours, right *y*-axis) contents in G_0 and G_4 particles from ICP-AES. The data were normalized to keep the sum of Mn/Co/Ni as 0.80. The error bars were calculated from the s.d. of the data in Supplementary Table 2. **c**, EELS line scan across a 400 nm particle and a representative EELS spectrum near the surface marked on the particle. Raw data are shown before background subtraction and so on with Gatan software. **d**, $X(r)$ profile (blue, left *y*-axis) and element percentages (other colours, right *y*-axis) from the surface to the bulk of a G_4 particle, calculated on the basis of EELS data from **c**. **e**, STEM-HAADF image of the Li-gradient region from $X(r_{surface}) = X_{poor} < 0$ to $X(r_{core}) = X_{rich} > 0$, showing a coherent lattice with $d_{(003)} = 0.473$ nm in both Li-rich and Li-poor regions, with M_{LiL} pillars (due to higher average *Z* of the atomic column) that disappear toward the core. The surface inclination here is different from that of Fig. 1e. **f**, Ratio of Mn L_3/L_2 peak area near the surface indicating valence change of Mn ions.

decomposition when encountering freed oxygen[24–26]. Since liquid electrolyte is only ~40 wt% of the cathode in industrial batteries, and because the anode, cathode and separator must be wet while also being consumed on the anode side, the electrolyte is often the most limiting resource in full-cell cycling. $LX_{(r)}MO$ should lead to better full-cell cycle life, which we will verify later in this article.

G_0, G_4 and G_6 were then tested in half-cells. As shown in Fig. 3b, in the first cycle under 0.1C (1C ≡ 250 mA g^{-1}), G_0 could be charged to 347.2 mAh g^{-1} but discharged only to 261.9 mAh g^{-1} with an initial Coulombic efficiency (CE) of 75.4%. G_4 could be charged to 322.8 mAh g^{-1}, but it could discharge to 293.1 mAh g^{-1} with a much higher initial CE of 90.8%. G_6 had an even higher initial CE of 91.4%, but it could be charged only to 305.9 mAh g^{-1} and discharged to 279.7 mAh g^{-1}. Thus, we should be aware that while increasing *w* and the amount of LiO extracted can improve the initial CE, one will also lose some capacity. So the amount of MoO_3 used in leaching needs to be optimized to balance the trade-off between discharge capacity and cycle life under parsimonious electrolyte condition. It is encouraging that the gradient $LX_{(r)}MO$ particles improved the first-cycle CE by >15%.

The charge/discharge profiles at 0.2C are shown in Fig. 3c and Supplementary Fig. 8. G_0 had seriously degraded discharge profiles after only 50 cycles. However, both the capacity and voltage were well retained for G_4, which kept very similar discharge profiles even after 200 cycles. The capacity, average discharge voltage and energy density retention are summarized in Fig. 3d. G_4 had not only much higher initial average discharge voltage and capacity (3.602 V, 280.7 mAh g^{-1}) than G_0 (3.533 V, 249.4mAh g^{-1}) but also much better capacity and voltage retention. After 200 cycles at 0.2C, G_4 maintained a discharge capacity of 250.4 mAh g^{-1} with 3.368 V average voltage, while G_0 retained only 198.5 mAh g^{-1} with 2.944 V average voltage. In terms of energy density, G_4 could reach 1,011 Wh kg^{-1} initially and still retained 892 Wh kg^{-1} after 100 cycles and 843 Wh kg^{-1} after 200 cycles, whereas G_0 had only 589 Wh kg^{-1} after 200 cycles. G_4 had enhanced capacity and voltage retention at other rates as well (Supplementary Figs. 8 and 9).

Voltage decay can be better understood by comparing the cyclic voltammetry (CV) between G_0 and G_4 in Fig. 3e,f: The oxidation peaks of G_0 and G_4 in the second cycle at 3.8 V and 4.2–4.6 V are dominated by $Ni^{2+/3+/4+}/Co^{3+/4+}$ cation oxidation and oxygen anion oxidation, respectively. After 50 cycles, the peak area of G_0 at high voltage in charging seriously decreased due to less oxygen anion oxidation, while that due to $Mn^{3+/4+}$ redox increased, inevitably downshifting the reduction peak to a lower voltage of ~3.0 V. Thus, the average discharge voltage of G_0 would continuously decay during cycling. However, for G_4 (Fig. 3f), both peaks of oxygen anion redox and $Mn^{3+/4+}$ redox remained almost unchanged after 50 cycles. This further confirmed that continuous oxygen loss was prevented in G_4, and no additional Mn^{3+} was generated in room-temperature cycling. In contrast, the departure of oxygen/LiO and the reduction of cation valence also happened in G_0 but, notably, during electrochemical cycling at room temperature, where severe structural disruptions and side reactions with the electrolyte occur; this was unlike in G_4 where most of the structural defects were annealed out preventively under a controlled high-temperature environment. This is like the difference between the rout of an army and an ordered retreat. The average charge and discharge voltages in the cycling can be found in Supplementary Fig. 10. Galvanostatic intermittent titration technique (GITT) analysis (Supplementary Fig. 11) indicated that G_4 had both well-maintained thermodynamic open-circuit voltage profiles and suppressed kinetic titration voltage drops after 150 cycles, while those of G_0 both decayed severely (Supplementary Discussion 2).

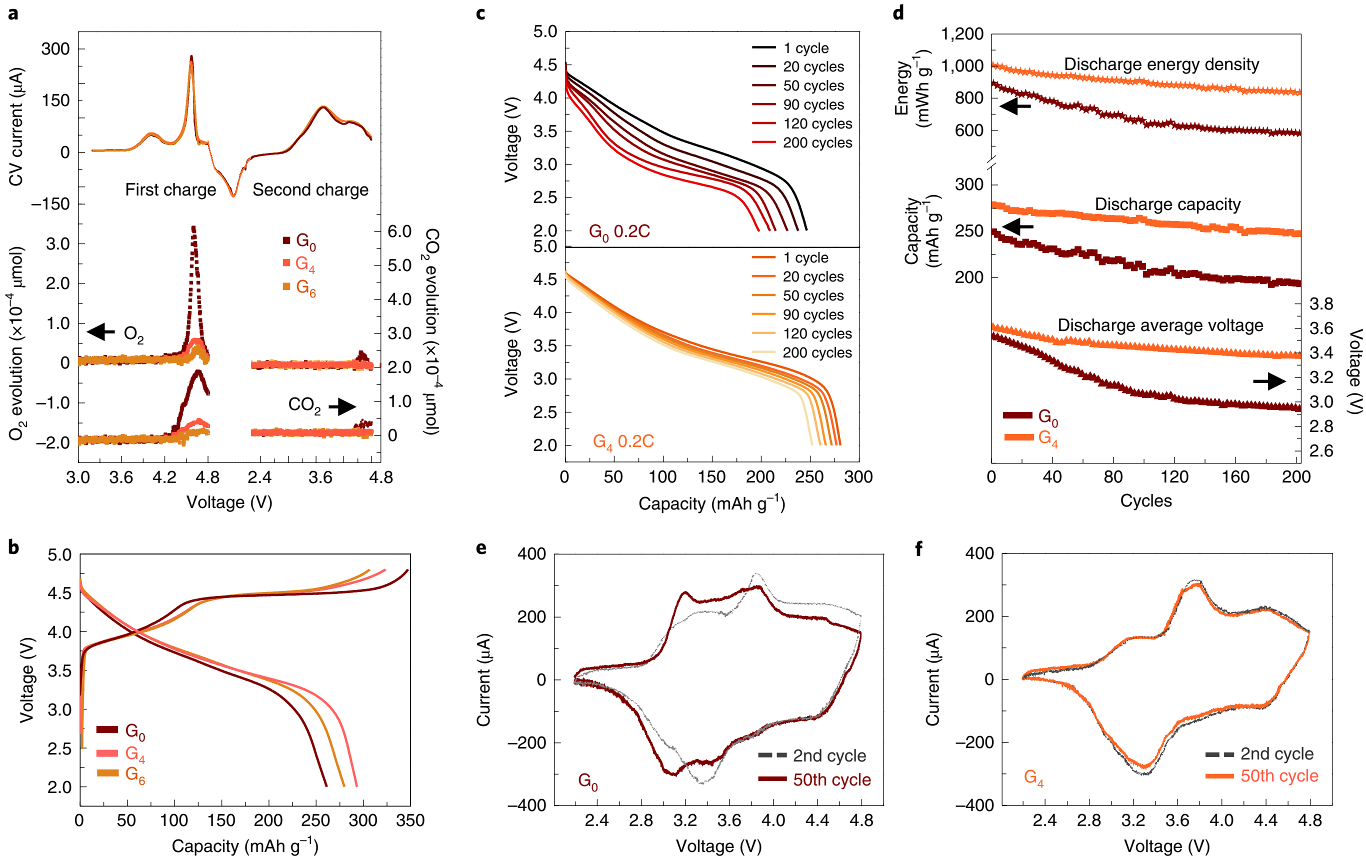

Fig. 3 | Electrochemical behaviours of the pristine $Li_{1.20}Mn_{0.48}Co_{0.16}Ni_{0.16}O_2$ and $Li_{1+X(r)}M_{1-X(r)}O_2$. **a**, DEMS of G_0, G_4 and G_6 in a CV test in a voltage range of 2.2–4.8 V with 0.1 mV s^{-1} scan rate. The weights of all G_0, G_4 and G_6 active materials were from 8.0 to 9.0 mg. The mass spectra of $m/z = 32$ for O_2 and $m/z = 44$ for CO_2 were collected in the initial two positive scanning sweeps. **b**, Charge/discharge profiles of G_0, G_4 and G_6 in the first cycle at 0.1C (1C ≡ 250 mA g^{-1}). **c**, Discharge profiles of G_0 and G_4 for 200 cycles at 0.2C and 25 °C after five formation cycles at 40 °C and 0.1C. **d**, Discharge capacity, average discharge voltage and energy density of G_0 and G_4 at 0.2C collected from **c**. **e**,**f**, CV of G_0 (**e**) and G_4 (**f**) in the 2nd and 50th cycles.

Stabilized Mn valence and phase in cycling

sXAS was performed to distinguish the oxidation states of elements in the bulk and at the surface of G_4 particles. The diameters of G_4 particles range between 200 and 400 nm, so the fluorescence yield (FY) mode with detection depth of 100 to ~200 nm can collect the information from r_{core}, whereas the total electron yield (TEY) mode displays only the information at the surface within a few nanometres depth[34]. The O K edge starting at 528 eV comes from the excitation of O_{1s} electrons to the hybridized M_{3d}–O_{2p} orbitals, which has been widely used to indicate the overall change of M–O oxidation states[12,35–37]. In Fig. 4a, by quantifying the intensity integral of the normalized sXAS O K edge peaks under FY and TEY modes at 527.5–534.2 eV, it can be confirmed that more electrons had been extracted from the Li-rich bulk ($\delta^+ = 1.05$, 329 mAh g^{-1}) than from the Li-poor surface ($\delta^+ = 0.81$, 221 mAh g^{-1}) in the initial charge (Supplementary Note 1).

Meanwhile, sXAS M $L_{3,2}$ edges are ideally suited to quantify the M valence in G_4[37–39]. Figure 4b,c shows the Mn and Ni sXAS L_3 edges before and after charge. It can be clearly seen that the Mn FY L_3 edge did not change (both being +4), while the TEY edge changed a lot after charge. Quantitative analysis[37–40] on TEY Mn L_3 edge (Fig. 4d) indicated that 5% Mn^{2+}, 54% Mn^{3+} and 41% Mn^{4+} (average Mn valence of +3.36) was contained in the Li-poor surface of G_4 particles before charge. After charging to 4.8 V, Mn^{4+} increased to 96%, Mn^{3+} decreased to 4%, and Mn^{2+} was totally gone (average Mn valence of +3.96). Therefore, Mn contributed no capacity in the Li-rich bulk, but 0.38e (0.63 × 0.6e) at the Li-poor surface while charging. Although quantitative valence analysis is difficult for Ni and Co ions because of the absence of standard Ni^{4+} and Co^{4+} material references, we can still see that both the Ni and Co valences increased a lot after charging, from both FY and TEY Ni sXAS L_3 edges (Fig. 4c and Supplementary Fig. 12; refs. [38,40]). However, in the $Li_{1.2}Mn_{0.48}Co_{0.16}Ni_{0.16}O_2$ bulk of G_4, even if all Ni and Co ions were oxidized to +4 after charging (see quantitative estimate in Supplementary Discussion 3 based on FY sXAS analysis, which reflects mainly the core, but also some surface information, thus slightly different from the illustrative Fig. 1a), M can supply at most $\delta^+ = 0.42e$ (= 132 mAh g^{-1}), and the remaining 0.63e (= 197 mAh g^{-1}) must come from oxygen anion redox, demonstrating the genuine HACR nature[1] when averaging over the $LX_{(r)}MO$ particle volume. In contrast, in just the $Li_{0.95}Mn_{0.63}Ni_{0.21}Co_{0.21}O_2$ surface region, even if all the 0.81e (= 221 mAh g^{-1}) is acquired from M redox, the Ni and Co ions were required to be oxidized to only about +3.52 after charge, which leaves room for them to reach higher valence before the oxidation of oxygen[37,40,41] needs to be initiated.

We also performed an EELS line scan on a charged particle prepared by focused ion beam to obtain the depth profile of oxygen oxidation states in a G_4 particle (Fig. 4e). It clearly shows that the split peak of the O K edge at 530 eV was isolated, with the peak at 532 eV at the surface, but peak A gradually grew stronger and enclosed peak B when moving to the bulk. It has been shown that peak A grows to enclose peak B only when O_{2p} contributes to capacity[12,35–37]. The EELS result provided additional qualitative support for the claim that oxygen was highly redox active in the bulk but

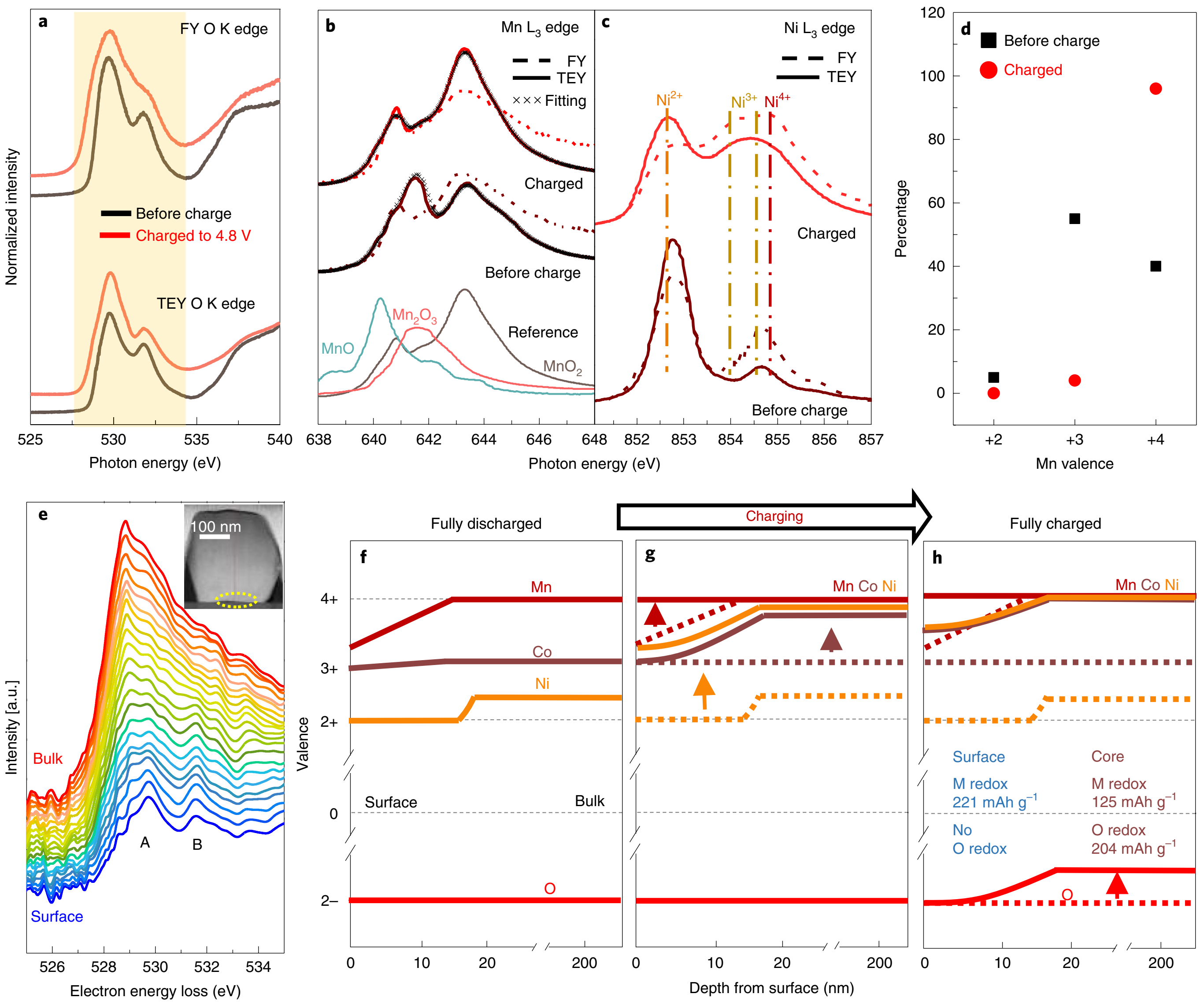

Fig. 4 | Valence profiles of oxygen and M in gradient LX$_{(r)}$MO in the charge process. **a**, Normalized (see Methods) sXAS O K edge of G_4 from discharged to charged states collected from FY and TEY modes. The normalized intensity was integrated from 527.5 eV to 534.2 eV, as indicated by the light orange background. **b**, sXAS Mn L_3 edge for discharged and charged states under FY and TEY modes. The TEY Mn L_3 edge was fitted by linear combination of Mn^{2+}, Mn^{3+} and Mn^{4+} TEY references. **c**, sXAS Ni L_3 edge for discharged and charged states under FY and TEY modes. **d**, Distribution of Mn valence at the surface for discharged and charged states. **e**, O K edge profiles from the surface to the bulk after charge, with EELS line scan. Inset: the charged particle after FIB. The yellow circle indicates where the EELS data were collected. **f–h**, Sketches of Mn, Ni, Co and O valence profiles from particle surface to bulk in G_4 during charging, which can also be found in Supplementary Video 1. This schematic is based on the hypothesis of 100% Co^{4+} and Ni^{4+} in the bulk when fully charged. The O anion redox can supply 204 mAh g^{-1} in the Li-rich bulk, while supplying no capacity at the Li-poor surface.

gradually became less oxidized and even totally unoxidized near the surface when charging. Thus Mn, Ni, Co and O oxidation state profiles throughout the G_4 particle in the charge process are shown schematically in Fig. 4f–h and Supplementary Video 1 (assuming that all Ni and Co ions can be oxidized to +4 in the Li-rich bulk). They show that O in r_{core} contributes significant capacity, but O in r_{surface} does not participate in anion redox, so the altered-valence oxygen mobility (that is, local oxygen mobility) can be limited to inside the particle.

The eliminated global oxygen mobility can stabilize Mn valence in battery cycling. Figure 5a shows the FY XAS Mn L edge of G_0 and G_4 before cycling and after 150 cycles. It clearly shows that even though Mn^{3+} was pre-positioned in the Li-poor surface of G_4, the amount of Mn^{3+} did not increase in G_4 after 150 cycles, while a massive amount of new Mn^{3+} was introduced in G_0 during cycling. Figure 5b,c shows high-resolution TEM images of G_0 and G_4 after 100 cycles. It can be clearly seen that for G_0, as many references have also reported[10,15,16], a great deal of structural damage and many phase transformations occurred, especially near the particle surface. By contrast, little phase transformation or structural collapse was found in G_4 after 100 cycles. The phase difference between G_0 and G_4 can be seen more explicitly from the XRD analysis after 150 cycles in Supplementary Fig. 13. From the STEM-HAADF image in Fig. 5d, we can see that M_{LiL} pillars (consistent with our density functional theory (DFT) simulation, Fig. 5d) were also well preserved after 100 cycles. Therefore, the coherent Li-gradient surface assisted by M_{LiL} pillars had effectively supported the layered structure, preventing ‘army rout’ during prolonged cycling.

Phase stabilization can significantly enhance the kinetics in cycling. With GITT, Li diffusivity $\left(\hat{D}_{\mathrm{Li}^+}\right)$ in the 3rd cycle and

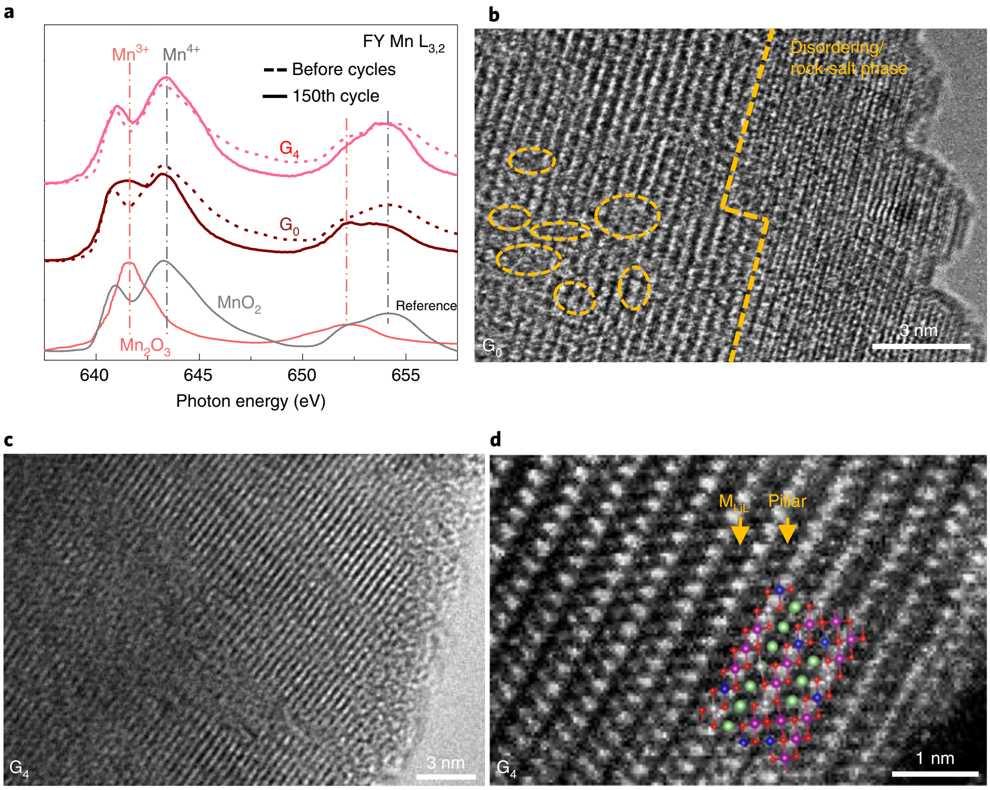

Fig. 5 | Mn oxidation states and structural damage after cycling. **a**, sXAS Mn $L_{3,2}$ edges of G_0 and G_4 before cycling and after 150 cycles in the FY mode and those of Mn^{3+} and Mn^{4+} references. **b**, HRTEM image of G_0 after 100 cycles; the regions on the right of the orange line and in circles indicate disordering/ rock-salt phase. **c**, HRTEM image of G_4 after 100 cycles. **d**, STEM-HAADF image of the G_4 surface region, indicating intact layered structure with M_{LiL} pillars in the Li layer after 100 cycles. The coloured structure is from the DFT simulation with Mn (violet), Co (grey), Ni (blue), Li (green) and O (red) atoms.

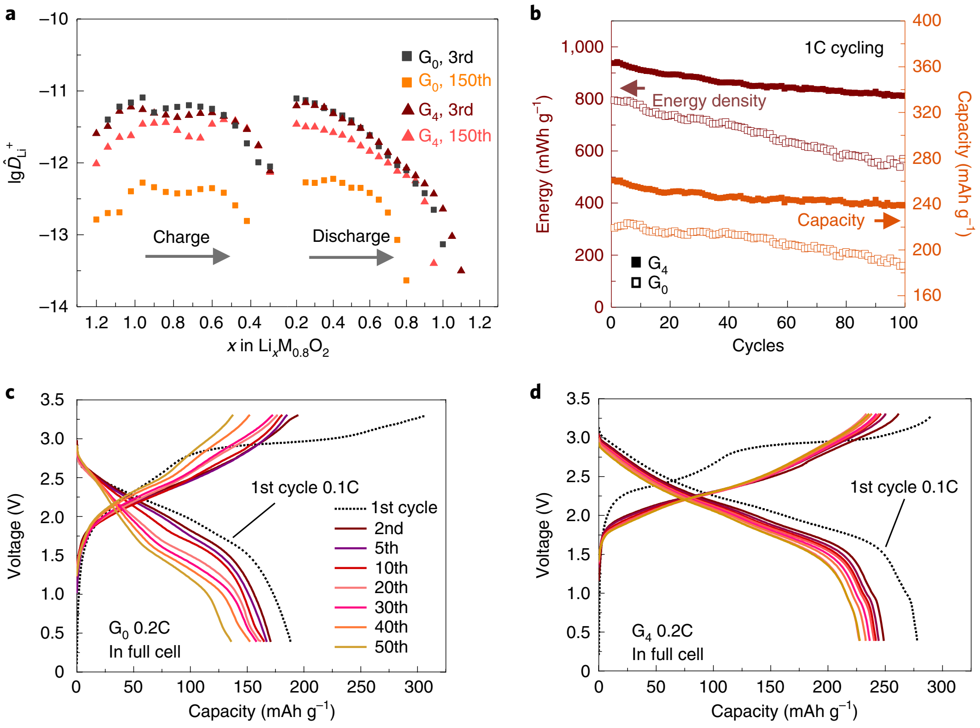

Fig. 6 | Stabilization of Li diffusivity and full-cell cycling. **a**, Average Li diffusivity in particles in the 3rd cycle and the 150th cycle of G_0 and G_4, measured by GITT at different states of charge. **b**, Discharge capacity and energy density of G_0 and G_4 in the initial 100 cycles in a half-cell under 1C. **c**,**d**, Charge/ discharge profiles of G_0 (**c**) and G_4 (**d**) in a full-cell battery against an $Li_4Ti_5O_{12}$ anode with only 2 g Ah^{-1} electrolyte (1 M $LiPF_6$ in EC/DEC with a volume ratio of 1:1, and 2 wt% vinylene carbonate).

the 150th cycle were compared between G_0 and G_4 in Fig. 6a and Supplementary Discussion 4. It can be seen that $\hat{D}_{Li^+}$ of G_0 degraded by nearly an order of magnitude after 150 cycles, while that of G_4 barely changed. Electrochemical impedance spectroscopy (Supplementary Fig. 14) showed that the charge-transfer resistance of G_4 was also significantly stabilized in cycling. The stabilized Li ion conductivity and interfacial impedance improved the cycling performance under higher rates. The cycling of G_0 and G_4 at 1C (Fig. 6b) showed that G_0 had a discharge capacity of 223.3 mAh g^{-1} at the beginning, but it quickly decreased to 188.2 mAh g^{-1} after 100 cycles. G_4 had a discharge capacity of 262.6 mAh g^{-1} at the beginning and still had discharge capacity of 238.0 mAh g^{-1} after 100 cycles. As shown in Fig. 6b, G_4 could discharge nearly 925 Wh kg^{-1} in the first cycle and retained 808 Wh kg^{-1} after 100 cycles, whereas G_0 could only discharge 793 Wh kg^{-1} at the beginning and faded to 571 Wh kg^{-1} after 100 cycles at 1C. Remarkably, for the 100th cycle under 1C, G_4 had 42% higher discharge energy density than G_0.

The minimized release of freed oxygen decreases side reactions and electrolyte consumption[42–46]. To simulate the operation of practical cells in industry, we used only ~2 g Ah^{-1} electrolyte in a capacity-matched full cell to see how many cycles the cells could survive. $Li_4Ti_5O_{12}$ was used as the anode to avoid side reactions with the very limited electrolyte. From Fig. 6c,d it can be seen that, although both G_0 and G_4 could be charged to ~300 mAh g^{-1} in the initial cycle, G_0 could only discharge to 188.1 mAh g^{-1} in the first cycle, and it decreased quickly to 132.3 mAh g^{-1} after 50 cycles at 0.2C. The consumption of liquid electrolyte due to reactions with the freed oxygen rapidly increased the impedance and dried out the full cell. In contrast, G_4 could discharge to 276.9 mAh g^{-1} in the first cycle and could still discharge to 225.5 mAh g^{-1} at 0.2C after 50 cycles. This means G_4 can work well in lean-electrolyte conditions prevalent in industrial batteries.

Conclusions

We developed a scalable solid-state synthesis method to produce Li-gradient $Li_{1+X(r)}M_{1-X(r)}O_2$ particles through a high-temperature LiO leaching by molten MoO_3. The bulk and the surface regions share a fully occupied oxygen framework without grain or phase boundaries or appreciable lattice defects. Particles with a high-energy-density core region that has excess axial Li–O–Li configurations and extra anion-redox activities are now individually wrapped by an epitaxially coherent surface region with no Li–O–Li axes and even some M–O–M axes configurations—that is, 'atomic pillars' that prevent structural collapse when Li is extracted—to prevent near-surface oxygen ions from participating in anion redox and gaining mobility. After that, only axial Li–O_{2p}–Li embedded inside the interior can be activated for HACR, which is akin to the Li_2O–LiO–LiO_2 cathode concept[2] but well mixed at the atomic scale. These oxygen ions are well trapped in the particle bulk due to the absence of percolating diffusion pathways to the surface (the concept of 'solid oxygen').

Our high-temperature surface treatment can be generalized to leach other elements to avoid unexpected surface reactions; for example, we may leach out Ni from Ni-rich NMC particles with other reagents that create a Ni-poor surface to reduce Li/Ni cation mixing during cycling. By further optimizing the amount of leaching agents, the temperature and the time of the reactions, one may obtain the transition metal gradient and Li-richness/poorness gradient profiles that enable the best electrochemical performance for HACR cathodes.

Methods

Synthesis of the uniformly Li-rich particles. The Li-rich $Li_{1.20}Mn_{0.48}Ni_{0.16}Co_{0.16}O_2$ material was prepared by a wet co-precipitation method followed by a solid-state reaction process. First, $MnSO_4$·H_2O (Reagent Plus, ≥99%, Sigma-Aldrich), $NiSO_4$·$6H_2O$ (ACS Reagent, ≥98%, Sigma-Aldrich) and $CoSO_4$·$7H_2O$ (Reagent Plus, ≥99%, Sigma-Aldrich) were completely dissolved in deionized water with a molar ratio of 3:1:1. Then 0.5 mol l^{-1} NaOH solution was titrated into the solution with stirring in an 80 °C water bath until the pH reached 8–10. Stirring was maintained for 2 h, and then the solution was cooled to room temperature in air. The sediments were separated from water by centrifugation and washed with water. This process was repeated three times. Subsequently the product was dried at 80 °C in a vacuum oven to obtain a powder precursor. After that, the precursor was heated at 400 °C for 3 h to obtain a black intermediate product, and then it was mixed with LiOH·H_2O (ACS Reagent, ≥98%, Sigma-Aldrich). Finally, the mixture was heated at 600 °C for 3 h and then at 900 °C for 10 h to obtain the uniformly Li-rich $Li_{1.20}Mn_{0.48}Ni_{0.16}Co_{0.16}O_2$ material G_0.

Creation of Li-gradient $LX_{(r)}MO$. $(NH_4)_6Mo_7O_{24}$·$4H_2O$ (4–6 wt%) was dissolved in deionized water, and the pH was adjusted to 8–10 with NH_3·H_2O. Then the as-prepared $Li_{1.20}Mn_{0.48}Ni_{0.16}Co_{0.16}O_2$ material was added to the solution and dispersed with high-power ultrasound for 1 h and then evaporated with stirring in an 80 °C water bath. The powder was milled for a while and heated at 300 °C for 2 h, then kept at 700 °C for 10 h. Then the product was milled again and dispersed in deionized water by ultrasound for 1 h, and the solid was separated by centrifugation. Finally, the solid was dried at 150 °C in a vacuum oven for 3 h to obtain the final product.

Characterizations. XRD was performed on a PANalytical X'Pert PRO X-ray diffractometer using a Cu target under 45 kV and 40 mA. The data were collected at 2° per minute and analysed with the HighScore Plus software. Scanning electron microscopy was performed on a Zeiss Merlin high-resolution scanning electron microscope. The sample for atomic resolution STEM imaging was prepared by focused ion beam lift-out using the FEI Helios 600 with a Ga ion source. A platinum layer was deposited on top of a particle to protect the cathode particle before the lift-out. The HAADF images in STEM are taken from the aberration-corrected JEOL JEM-ARM200F operated under 200 keV, equipped with a cold field emission source. The probe convergence angle on a sample is 23 mrad, with the inner and outer diameters of the HAADF detector being 68 mrad and 280 mrad, respectively. The 2 K images (2,048 × 2,048 pixels) were acquired with a dwell time of 16 μs $pixel^{-1}$. EELS spectra were acquired using an FEI Talos F200X scanning/transmission electron microscope (200 kV) at the Center for Functional Nanomaterials, Brookhaven National Laboratory and using the aberration-corrected JEOL JEM-ARM200F, both with a dual EELS spectrometer. We used dual EELS to collect both the low-loss and high-loss spectra, and the low-loss spectra were utilized to correct the drift of the zero-loss peak. Based on the full-width at half-maximum of the zero-loss peak, the optimal energy resolution of EELS is about 0.7 eV. The EELS data were analyzed and processed with Gatan software. HRTEM images were taken on a JEOL 2010F at 200 kV. Local chemical analysis was performed using STEM-EDS with a HAADF detector.

sXAS measurements were carried out at the IOS (23-ID-2) beamline at the National Synchrotron Light Source II at Brookhaven National Laboratory. Spectra were acquired in total electron yield (TEY) and fluorescence yield (FY) modes. The estimated incident X-ray energy resolution was ~0.05 eV at the O K edge. The monochromator absorption features and beam instabilities were normalized by dividing the detected PFY and TEY signals by the drain current of a clean gold I0 mesh placed in the incident beam. TEY spectra were recorded from the drain current of the sample and PFY data were acquired using a Vortex-EM silicon drift detector. The sXAS spectra for the O K edge were recorded over a wide energy range, from 520 to 565 eV, covering energies well below and above sample absorptions. The normalization of the O K edge was performed[12] as follows. (1) I0 normalization: the sample signal is divided by the incident intensity measured from the sample drain current from a freshly coated gold mesh inserted into the beam path before the X-rays can impinge on the sample. (2) A linear, sloping background is removed by fitting a line to the flat, low-energy region (520–524 eV) of the sXAS spectrum. (3) The spectrum is normalized by setting the flat, low-energy region to zero and the post-edge to unity (unit edge jump). The photon energy selected for the post-edge was 560 eV, beyond the region of any absorption (peaks).

Electrochemical test. R2032 coin cells were used for the electrochemical tests in this work. Half-cells were fabricated from a cathode of 80 wt% active material, 10 wt% carbon black and 10 wt% polyvinylidene fluoride (PVDF) binder, which was pasted on an Al current collector at a loading of 10 mg cm^{-2}; an anode of Li metal sheets; a separator of Celgard 2400 polymer; and a commercial electrolyte solution of 1 M $LiPF_6$ dissolved in a mixture of ethylene carbonate (EC) and diethyl carbonate (DEC) with a volume ratio of 1:1 and 2 wt% vinylene carbonate additive. A Land CT2001A 8-channel automatic battery test system (Wuhan Lanhe Electronics) was used for charging/discharging of the cells. An electrochemical workstation (Gamry Instruments, Reference 3000) was used for the CV scan between 2.2–4.8 V. GITT was also performed on the electrochemical workstation with constant current for 200 s followed by 1,800 s relaxation with an upper voltage of 4.8 V and a lower limit of 2.0 V. Electrochemical impedance spectroscopy was performed between 0.1 Hz and 1 MHz with a 10 mV amplitude. The electrochemical tests were all carried out at room temperature. A homemade quantitative spectrometer for DEMS was used to detect and analyse the gas during the cell testing. Two glued polyether ether ketone (PEEK) capillary tubes were used for inlet and outlet of gas. The cell was fabricated in a glove box where $O_2 < 0.1$ ppm. Then, the output tube was connected to a commercial Thermo Scientific mass spectrometer. High-purity argon gas was used as the carrier gas with a flow rate of 3 ml min^{-1} during the cycling process. In the CV process, the scan rate was 0.05 mV s^{-1}, and mass spectrometer spectra were collected every 30 s.

First-principles calculation. The calculation is performed using density functional theory (DFT) within the spin-polarized generalized gradient approximation (GGA) including the on-site Coulomb interaction correction (GGA + U), in the form of the Perdew–Burke–Ernzerhof's exchange-correlation functional. The code is implemented in the Vienna Ab initio Simulation Package (VASP). The planewave energy cut-off is 400 eV. The U values of Mn, Co and Ni are 3.9, 3.3 and 6.2 eV, respectively.

Data availability

The data that support the plots in this paper and other findings of this study are available from the corresponding author upon reasonable request.

Received: 26 February 2019; Accepted: 22 October 2019;
Published online: 12 December 2019

References

1. Xue, W. et al. Intercalation-conversion hybrid cathodes enabling Li–S full-cell architectures with jointly superior gravimetric and volumetric energy densities. *Nat. Energy* **4**, 374–382 (2019).
2. Zhu, Z. et al. Anion-redox nanolithia cathodes for Li-ion batteries. *Nat. Energy* **1**, 16111 (2016).
3. Qiao, Y., Jiang, K. Z., Deng, H. & Zhou, H. S. A high-energy-density and long-life lithium-ion battery via reversible oxide–peroxide conversion. *Nat. Catal.* **2**, 1035–1044 (2019).
4. Kim, S., Cho, W., Zhang, X., Oshima, Y. & Choi, J. W. A stable lithium-rich surface structure for lithium-rich layered cathode materials. *Nat. Commun.* **7**, 13598 (2016).
5. Luo, K. et al. One-pot synthesis of lithium-rich cathode material with hierarchical morphology. *Nano Lett.* **16**, 7503–7508 (2016).
6. Yu, H. J. & Zhou, H. S. High-energy cathode materials (Li_2MnO_3–$LiMO_2$) for lithium-ion batteries. *J. Phys. Chem. Lett.* **4**, 1268–1280 (2013).
7. Yu, H. J. et al. High-energy 'composite' layered manganese-rich cathode materials via controlling Li_2MnO_3 phase activation for lithium-ion batteries. *Phys. Chem. Chem. Phys.* **14**, 6584–6595 (2012).
8. Ye, D. L. et al. Understanding the origin of Li_2MnO_3 activation in Li-rich cathode materials for lithium-ion batteries. *Adv. Fun. Mater.* **25**, 7488–7496 (2015).
9. Seo, D.-H. et al. The structural and chemical origin of the oxygen redox activity in layered and cation-disordered Li-excess cathode materials. *Nat. Chem.* **8**, 692–697 (2016).
10. Yan, P. et al. Injection of oxygen vacancies in the bulk lattice of layered cathodes. *Nat. Nanotechnol.* **14**, 602–608 (2019).
11. Lee, E. & Persson, K. A. Structural and chemical evolution of the layered Li-excess Li_xMnO_3 as a function of Li content from first-principles calculations. *Adv. Energy Mater.* **4**, 1400498 (2014).
12. Luo, K. et al. Charge-compensation in 3*d*-transition-metal-oxide intercalation cathodes through the generation of localized electron holes on oxygen. *Nat. Chem.* **8**, 684–691 (2016).
13. Lee, J. Y. et al. Mitigating oxygen loss to improve the cycling performance of high capacity cation-disordered cathode materials. *Nat. Commun.* **8**, 981 (2017).
14. Chen, H. R. & Islam, M. S. Lithium extraction mechanism in Li-rich Li_2MnO_3 involving oxygen hole formation and dimerization. *Chem. Mater.* **28**, 6656–6663 (2016).
15. Singer, A. et al. Nucleation of dislocations and their dynamics in layered oxide cathode materials during battery charging. *Nat. Energy* **3**, 641–647 (2018).
16. Hu, E. Y. et al. Evolution of redox couples in Li- and Mn-rich cathode materials and mitigation of voltage fade by reducing oxygen release. *Nat. Energy* **3**, 690–698 (2018).
17. Hy, S., Felix, F., Rick, J., Su, W. N. & Hwang, B. J. Direct in situ observation of Li_2O evolution on Li-rich high-capacity cathode material, $Li[Ni_xLi_{(1-2x)/3}Mn_{(2-x)/3}]O_2$ $(0 \le x \le 0.5)$. *J. Am. Chem. Soc.* **136**, 999–1007 (2014).
18. Tran, N. et al. Mechanisms associated with the "plateau" observed at high voltage for the overlithiated $Li_{1.12}(Ni_{0.425}Mn_{0.425}Co_{0.15})_{0.88}O_2$ system. *Chem. Mater.* **20**, 4815–4825 (2008).
19. Yan, P. F. et al. Probing the degradation mechanism of Li_2MnO_3 cathode for Li-ion batteries. *Chem. Mater.* **27**, 975–982 (2015).
20. Guo, S. H. et al. Surface coating of lithium-manganese-rich layered oxides with delaminated MnO_2 nanosheets as cathode materials for Li-ion batteries. *J. Mater. Chem. A* **2**, 4422–4428 (2014).
21. Zheng, F. H. et al. Nanoscale surface modification of lithium-rich layered-oxide composite cathodes for suppressing voltage fade. *Angew. Chem. Int. Ed.* **54**, 13058–13062 (2015).
22. Kang, S. H., Johnson, C. S., Vaughey, J. T., Amine, K. & Thackeray, M. M. The effects of acid treatment on the electrochemical properties of $0.5\,Li_2MnO_3 \bullet 0.5\,LiNi_{0.44}Co_{0.25}Mn_{0.31}O_2$ electrodes in lithium cells. *J. Electrochem. Soc.* **153**, A1186–A1192 (2006).
23. Qiu, B. et al. Gas–solid interfacial modification of oxygen activity in layered oxide cathodes for lithium-ion batteries. *Nat. Commun.* **7**, 12108 (2016).
24. Bruce, P. G., Freunberger, S. A., Hardwick, L. J. & Tarascon, J. M. Li–O_2 and Li–S batteries with high energy storage. *Nat. Mater.* **11**, 19–29 (2012).
25. Freunberger, S. A. et al. Reactions in the rechargeable lithium–O_2 battery with alkyl carbonate electrolytes. *J. Am. Chem. Soc.* **133**, 8040–8047 (2011).
26. McCloskey, B. D., Bethune, D. S., Shelby, R. M., Girishkumar, G. & Luntz, A. C. Solvents' critical role in nonaqueous lithium–oxygen battery electrochemistry. *J. Phys. Chem. Lett.* **2**, 1161–1166 (2011).
27. Sun, Y.-K. et al. Nanostructured high-energy cathode materials for advanced lithium batteries. *Nat. Mater.* **11**, 942–947 (2012).
28. Lim, B. B. et al. Advanced concentration gradient cathode material with two-slope for high-energy and safe lithium batteries. *Adv. Funct. Mater.* **25**, 4673–4680 (2015).
29. Nakamura, T. et al. Defect chemical studies on oxygen release from the Li-rich cathode material $Li_{1.2}Mn_{0.6}Ni_{0.2}O_{2-\delta}$. *J. Mater. Chem. A* **7**, 5009–5019 (2019).
30. Cho, Y., Oh, P. & Cho, J. A new type of protective surface layer for high-capacity Ni-based cathode materials: nanoscaled surface pillaring layer. *Nano Lett.* **13**, 1145–1152 (2013).
31. Loomer, D. B., Al, T. A., Weaver, L. & Cogswell, S. Manganese valence imaging in Mn minerals at the nanoscale using STEM-EELS. *Am. Mineral.* **92**, 72–79 (2007).
32. Li, Z. P. et al. Interface and surface cation stoichiometry modified by oxygen vacancies in epitaxial manganite films. *Adv. Funct. Mater.* **22**, 4312–4321 (2012).
33. Lu, J. et al. Nanoscale coating of $LiMO_2$ (M = Ni, Co, Mn) nanobelts with Li^+-conductive Li_2TiO_3: toward better rate capabilities for Li-ion batteries. *J. Am. Chem. Soc.* **135**, 1649–1652 (2013).
34. Qiao, R. et al. Direct experimental probe of the Ni(II)/Ni(III)/Ni(IV) redox evolution in $LiNi_{0.5}Mn_{1.5}O_4$ electrodes. *J. Phys. Chem. C.* **119**, 27228–27233 (2015).
35. Luo, K. et al. Anion redox chemistry in the cobalt free 3*d* transition metal oxide intercalation electrode $Li[Li_{0.2}Ni_{0.2}Mn_{0.6}]O_2$. *J. Am. Chem. Soc.* **138**, 11211–11218 (2016).
36. Oishi, M. et al. Direct observation of reversible oxygen anion redox reaction in Li-rich manganese oxide, Li_2MnO_3, studied by soft X-ray absorption spectroscopy. *J. Mater. Chem. A* **4**, 9293–9302 (2016).
37. Dai, K. H. et al. High reversibility of lattice oxygen redox quantified by direct bulk probes of both anionic and cationic redox reactions. *Joule* **3**, 518–541 (2019).
38. Qiao, R. M. et al. Direct evidence of gradient Mn(II) evolution at charged states in $LiNi_{0.5}Mn_{1.5}O_4$ electrodes with capacity fading. *J. Power Sources* **273**, 1120–1126 (2015).
39. Risch, M. et al. Redox processes of manganese oxide in catalyzing oxygen evolution and reduction: an in situ soft X-ray absorption spectroscopy study. *J. Phys. Chem. C.* **121**, 17682–17692 (2017).
40. Li, Q. H. et al. Quantitative probe of the transition metal redox in battery electrodes through soft X-ray absorption spectroscopy. *J. Phys. D.* **49**, 413003 (2016).
41. Venkatraman, S., Shin, Y. & Manthiram, A. Phase relationships and structural and chemical stabilities of charged $Li_{1-x}CoO_{2-\delta}$ and $Li_{1-x}Ni_{0.85}Co_{0.15}O_{2-\delta}$ cathodes. *Electrochem. Solid State Lett.* **6**, A9–A12 (2003).
42. Hatsukade, T., Schiele, A., Hartmann, P., Brezesinski, T. & Janek, J. Origin of carbon dioxide evolved during cycling of nickel-rich layered NCM cathodes. *ACS Appl. Mater. Interfaces* **10**, 38892–38899 (2018).
43. Imhof, R. & Novak, P. Oxidative electrolyte solvent degradation in lithium-ion batteries: an in situ differential electrochemical mass spectrometry investigation. *J. Electrochem. Soc.* **146**, 1702–1706 (1999).
44. Jung, R., Metzger, M., Maglia, F., Stinner, C. & Gasteiger, H. A. Oxygen release and its effect on the cycling stability of $LiNi_xMn_yCo_zO_2$ (NMC) cathode materials for Li-ion batteries. *J. Electrochem. Soc.* **164**, A1361–A1377 (2017).
45. Wang, H. et al. CO_2 and O_2 evolution at high voltage cathode materials of Li-ion batteries: a differential electrochemical mass spectrometry study. *Anal. Chem.* **86**, 6197–6201 (2014).
46. de Biasi, L. et al. Chemical, structural, and electronic aspects of formation and degradation behavior on different length scales of Ni-rich NCM and Li-rich HE-NCM cathode materials in Li-ion batteries. *Adv. Mater.* **31**, 1900985 (2019).

Acknowledgements

We acknowledge the support from NSF ECCS-1610806 and Wuxi Weifu High-Technology Group Co., Ltd. This research used resources of the Center for Functional Nanomaterials and the 23-ID-2 (IOS) beamline of the National Synchrotron Light Source II, both of which are US Department of Energy Office of Science user facilities at Brookhaven National Laboratory, under contract DE-SC0012704. Also, this work was performed in part at the Center for Nanoscale Systems, a member of the National Nanotechnology Coordinated Infrastructure Network supported by the National Science Foundation under NSF award no. 1541959.

Author contributions

Z.Z. and J.Li conceived and designed the experiments. Z.Z. synthesized the materials and performed the electrochemical tests. D.Y, Y.Y. and B.W. performed the HRTEM imaging, STEM-EDS mapping, EELS line scan and focused ion beam sample preparation for aberration-corrected STEM characterizations. C.S. took aberration-corrected STEM images and performed the DFT calculations. D.Y., I.W. and A.H. measured the soft X-ray absorption. Z.Z., D.Y. and X.Y. did the sXAS data analysis. Z.Z. and J.Li wrote the paper. All authors analysed the data, discussed the results and commented on the manuscript.

Competing interests

The authors declare no competing interests.

Additional information

Supplementary information is available for this paper at https://doi.org/10.1038/s41560-019-0508-x.

Correspondence and requests for materials should be addressed to J.L.

Reprints and permissions information is available at www.nature.com/reprints.

Publisher's note Springer Nature remains neutral with regard to jurisdictional claims in published maps and institutional affiliations.

LI-ION BATTERIES

Li gradients for Li-rich cathodes

Developing high capacity yet stable cathodes is key to advancing Li-ion battery technologies. Now, a new metal oxide cathode that is rich in Li with a gradient in Li concentration is shown to be stable to O_2 release leading to long cycle life and high capacity.

Michael F Toney

The key to the widespread adoption of electric vehicles (EVs) is the battery, which requires improvements in price, driving range, charging time and operational safety[1]. Driving range is dependent on the energy stored within the battery and must be increased to avoid consumer range anxiety. Meanwhile, battery chemistries need to be based on Earth abundant elements to be manufactured at the scale required for a global transportation fleet. The positive electrode (cathode) for many EVs presently uses chemistries based on transition metal oxides, $LiMO_2$, where M represents a combination of Ni, Mn, Co and Al, with Li to transition metal ratios of 1:1. However, these cathodes are limited in terms of energy storage capacities (<200 mAh g^{-1}), while the use of high amounts of Co brings high cost and environmental and societal concerns. Much research has been devoted to improving the cathode by considering Li-rich transition-metal oxides[2], $Li_{1+r}M_{1-r}O_2$, where r is between 1 and ~1.3 and the Li to transition metal ratio is ~1.5. These have been shown to provide higher capacities (>250 mAh g^{-1}), because of the contribution from both cation and anion (oxygen) redox reactions[3], and to use less Co. However, these Li-rich oxides suffer from sustained loss of voltage (voltage fade) and loss of lattice oxygen (associated with the oxygen redox) over long-term cycling (Fig. 1a)[4], significantly limiting the actual capacity in an EV application.

To address these challenges, researchers have utilized metal oxide coatings and surface treatments on the particles that make up the cathode[5], but these have not adequately improved the cyclability and voltage fade. Writing in *Nature Energy*, Ju Li and co-workers at the Massachusetts Institute of Technology and Brookhaven National Laboratory[6] have reported cathode particles that have a stable gradient in Li concentration from Li rich in the core to Li poor in the shell, as illustrated in Fig. 1b. These cathodes are shown to largely eliminate the release of O_2, to provide stable oxygen redox and to have good cyclability up to 200 charge/discharge cycles.

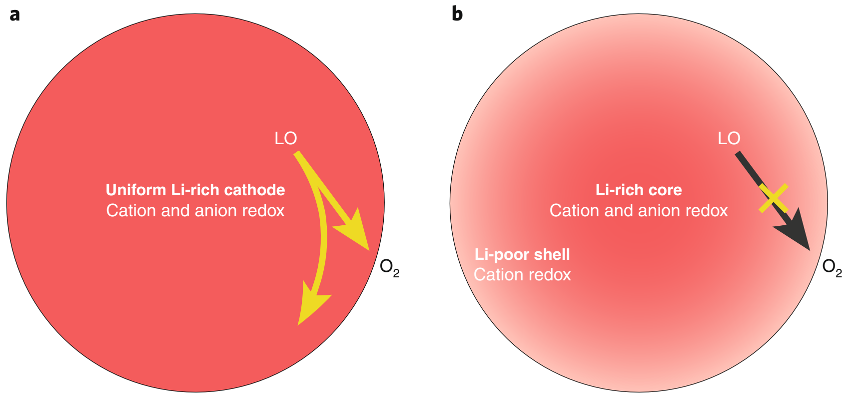

Fig. 1 | Schematics of Li-rich transition metal oxide cathode particles. **a**, In conventional Li-rich cathode particles, both cation and oxygen redox take place, leading to the loss of O_2, primarily from near the particle surface. **b**, In the Li-gradient particle of Li and colleagues, the Li-poor shell is stable and there is negligible O_2 loss because of the absence of O redox, resulting in enhanced cycling. LO represents lattice oxygen.

The synthesis of such stable Li-gradient core–shell particles is a challenging task, because Li could diffuse rapidly in the particles. Using a baseline oxide of Li-rich $Li_{1+r}(Mn_{0.6}Co_{0.2}Ni_{0.2})_{1-r}O_2$, with $r = 0.2$, Li and co-workers synthesize Li-gradient particles with a high temperature process involving a liquid MoO_3 that reacts with the near-surface region of an initially uniform transition-metal oxide particle and thus removes Li only from the particle shell. The high temperature has the advantage of annealing out any defects created during the Li extraction and results in a dense shell. Li and co-workers use a suite of characterization methods to show that the core retains the excess Li ($r = 0.20$) while the shell is Li poor ($r = -0.05$) (Fig. 1b).

Using differential electrochemical mass spectrometry, Li and co-workers showed that the Li-gradient cathodes exhibit no detectable O_2 loss after the first cycle, although a small loss of O_2 that is below the detection limit cannot be eliminated. Half cells of the Li-gradient cathodes were cycled and much reduced voltage and capacity fade was observed over 200 cycles relative to conventional Li-rich cathodes. Full cell tests (with $Li_4Ti_{15}O_{12}$ rather than conventional graphite anodes) further confirmed this improved stability up to 100 cycles. Both X-ray and electron spectroscopies were used to probe the oxygen and transition metals oxidation state in the core and shell. In the Li-rich core, the oxygen contributes to the redox behaviour in addition to the Ni and Co cation redox, which is similar to the case of other Li-rich particles. In contrast, in the Li-poor shell the oxygen does not show any redox reaction, while the redox behaviour is primarily the Ni and Mn cations. These results explain the improved voltage and capacity stability in the Li-gradient structure.

The research by Li and co-workers is a clear advance in enabling stable, high energy density cathode chemistries, but the adoption of these materials is still at an early stage. It remains to be seen if the high temperature, liquid MoO_3 based synthesis technique can be scaled up to a manufacturable level. Another challenge for this approach is to demonstrate stability up to ~ thousands of cycles as needed for practical EV applications, including the additional battery requirements created by autonomous 'vehicles as a service'. The composition used by Li and co-workers contains about 20% Co (per formula unit) and this is large compared to other potential cathode chemistries such as $LiNi_{0.9}Co_{0.05}Mn_{0.05}O_2$ that are hotly being pursued. Therefore, eliminating the problematic O_2 release with the Li-gradient and simultaneously reducing the Co content would be an idea solution. ❐

Michael F Toney
Stanford Synchrotron Radiation Light Source, Joint Center for Energy Storage Research, SLAC National Acceleratory Laboratory, Menlo Park, CA, USA.
e-mail: *mftoney@slac.stanford.edu*

https://doi.org/10.1038/s41560-019-0522-z

References

1. Crabtree, G. *Science* **366**, 422–424 (2019).
2. Li, B. & Xia, D. *Adv. Mater.* **29**, 1701054 (2017).
3. Yang, W. *Nat. Energy* **3**, 619–620 (2018).
4. Hu, E. et al. *Nat. Energy* **3**, 690–698 (2018).
5. Guo, S. et al. *J. Mater. Chem. A* **2**, 4422–4428 (2014).
6. Zhu, Z. et al. *Nat. Energy.* https://doi.org/10.1038/s41560-019-0508-x (2019).

nature energy

SUPPLEMENTARY INFORMATION

https://doi.org/10.1038/s41560-019-0508-x

In the format provided by the authors and unedited.

Gradient Li-rich oxide cathode particles immunized against oxygen release by a molten salt treatment

Zhi Zhu[1], Daiwei Yu[2], Yang Yang[1], Cong Su[1], Yimeng Huang[1], Yanhao Dong[1], Iradwikanari Waluyo[3], Baoming Wang[4], Adrian Hunt[3], Xiahui Yao[1], Jinhyuk Lee[1], Weijiang Xue[1] and Ju Li[1]*

---

[1]Department of Nuclear Science and Engineering and Department of Materials Science and Engineering, Massachusetts Institute of Technology, Cambridge, MA, USA. [2]Department of Electrical Engineering and Computer Science, Massachusetts Institute of Technology, Cambridge, MA, USA. [3]National Synchrotron Light Source II, Brookhaven National Laboratory, Upton, NY, USA. [4]Materials Research Laboratory, Massachusetts Institute of Technology, Cambridge, MA, USA. *e-mail: liju@mit.edu

Supplementary Information

Gradient Li-rich oxide cathode particles immunized against oxygen release by a molten salt treatment

Zhi Zhu[1], Daiwei Yu[2], Yang Yang[1], Cong Su[1], Yimeng Huang[1], Yanhao Dong[1], Iradwikanari Waluyo[3], Baoming Wang[4], Adrian Hunt[3], Xiahui Yao[1], Jinhyuk Lee[1], Weijiang Xue[1], and Ju Li[1*]

[1]Department of Nuclear Science and Engineering and Department of Materials Science and Engineering, Massachusetts Institute of Technology, Cambridge, Massachusetts 02139, USA.
[2]Department of Electrical Engineering and Computer Science, Massachusetts Institute of Technology, Cambridge, Massachusetts 02139, USA.
[3]National Synchrotron Light Source II, Brookhaven National Laboratory, Upton, NY 11973
[4]Materials Research Laboratory, Massachusetts Institute of Technology, Cambridge, Massachusetts 02139, USA.

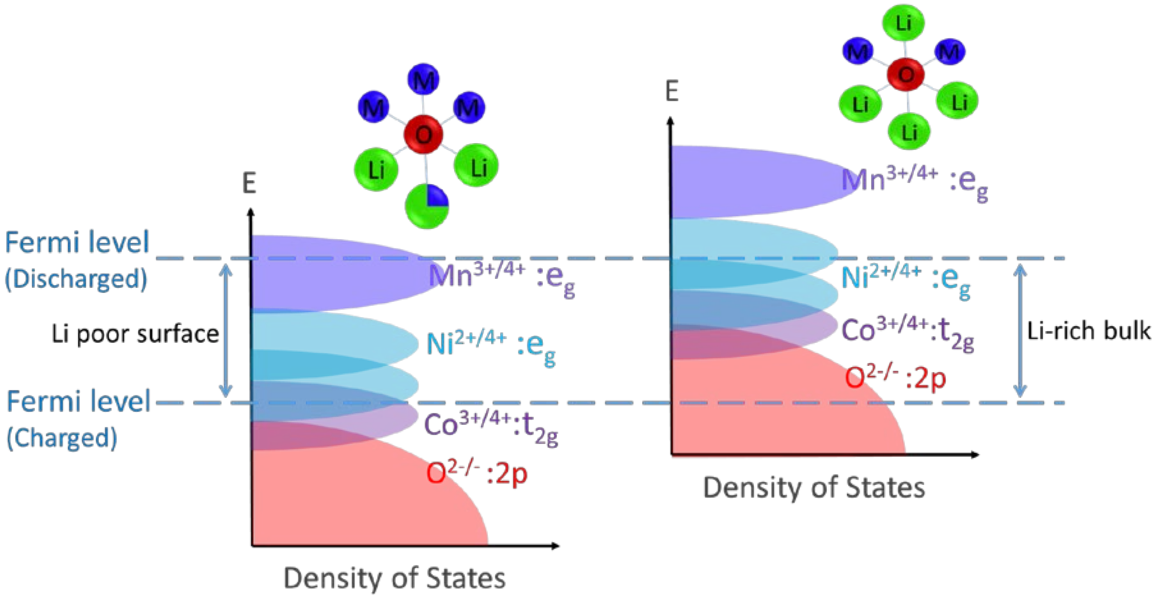

Supplementary Figure 1. Electronic band structure of the Li-poor surface (left) and the Li-rich bulk (right)

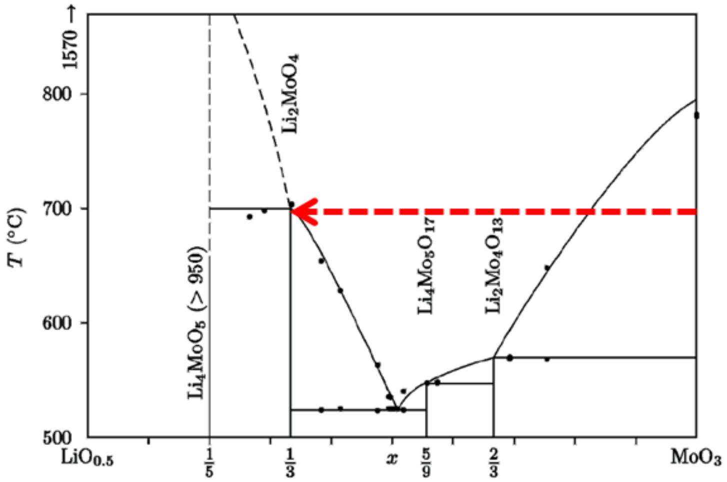

Supplementary Figure 2. Phase diagram of Li_2O and MoO_3[1] and the phase change route (red arrow) from MoO_3 to final Li_2MoO_4. Upon heating at 650-750 ºC, MoO_3 kept solid state at the beginning. After some $LiO_{0.5}$ was leached, the solid solution turned into liquid, which then uniformly wetted and wrapped around the Li-rich particle surface. $LiO_{0.5}$-MoO_3 remained in a liquid phase as more $LiO_{0.5}$ was leached. When $LiO_{0.5}$:MoO_3 = 2, saturation was reached and no more $LiO_{0.5}$ can be leached out. The final product wrapped on the particle surfaces is Li_2MoO_4.

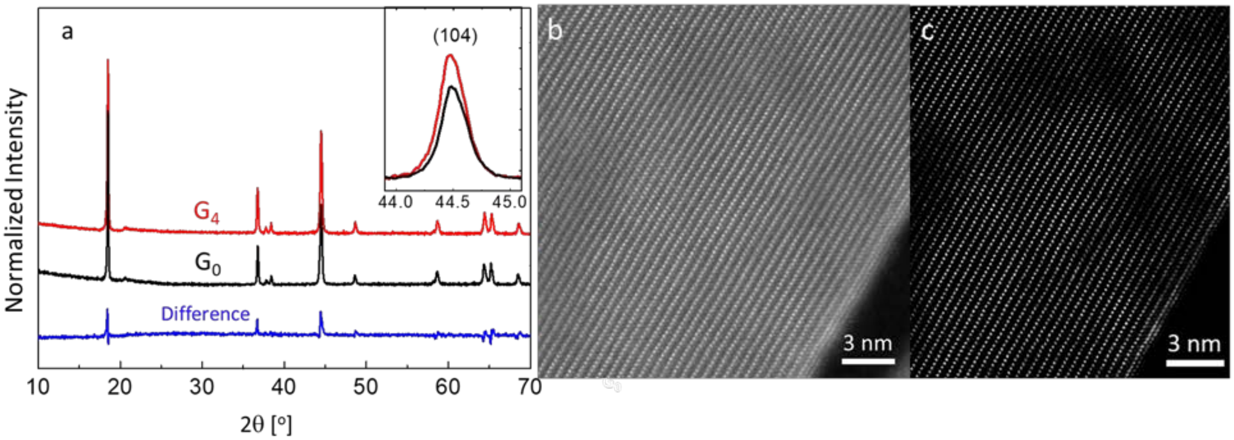

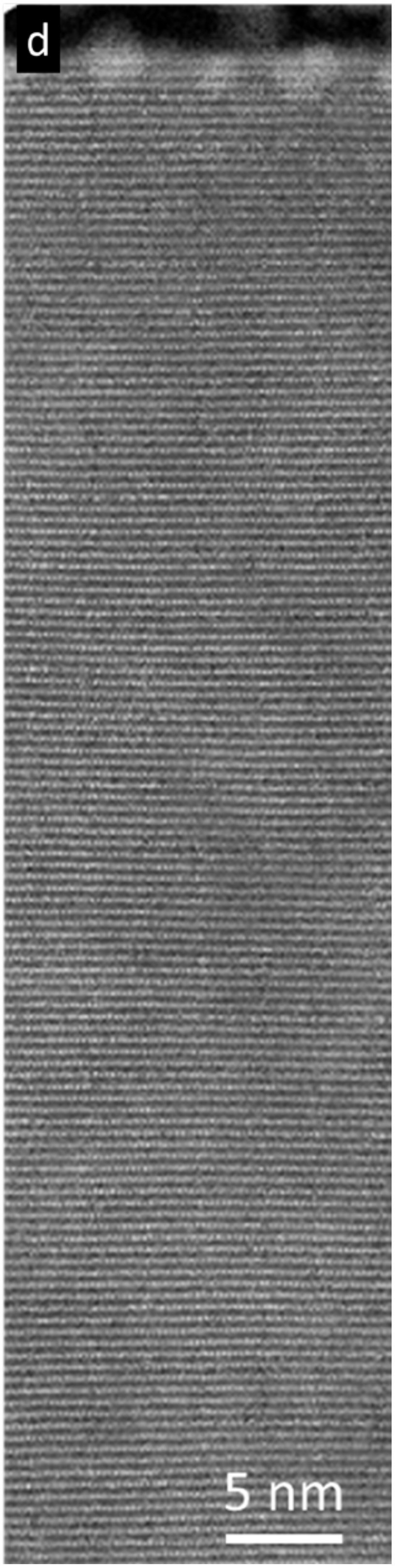

Supplementary Figure 3. (a) XRD patterns of G_0 and G_4, the patterns were normalized with their respective (003) peaks, both set as 1. The two patterns had little difference except the intensity ratio of

I(003)/(104) while no peak splitting nor peak shift was observed for both G_0 and G_4. (b) Raw image of STEM-HAADF image of G_0 and (c) Contrast-enhanced image of (b) to highlight the layered M lattice. (d) HRTEM image of G_4, showing atomic layers from the surface to tens of nanometers deep.

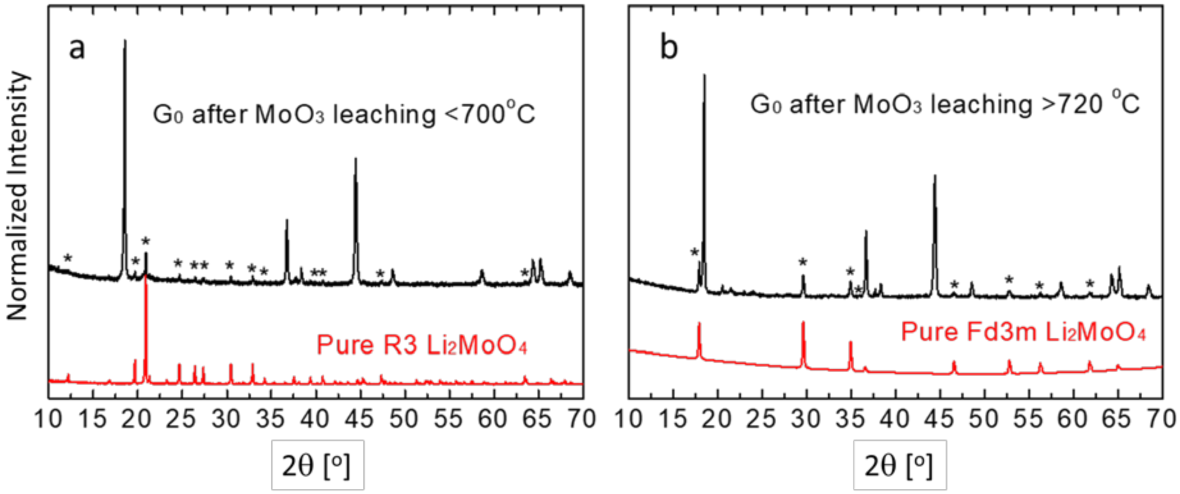

Supplementary Figure 4. XRD patterns of the intermediate product after MoO_3 leaching (a) at ≤700 °C and (b) at ≥720 °C. The new peaks after MoO_3 leaching at ≤700 °C (a) were totally matched with the one of pure Li_2MoO_4 (Sigma-Aldrich, >99.9%), which has R3h crystal structure (sd_1801711). The main peak (highest intensity) was at 2θ=20.9°, due to (211) lattice with *d*=4.29Å. The new peaks in G_0 after MoO_3 leaching at ≥720 °C (b) were well matched with the one of pure Li_2MoO_4 with spinel Fd3m crystal structure (sd_0307446). Though we cannot get nor prepare such pure Li_2MoO_4 product at present, we can still get the reference from[2] (https://materials.springer.com/isp/crystallographic/docs/sd_0307446)

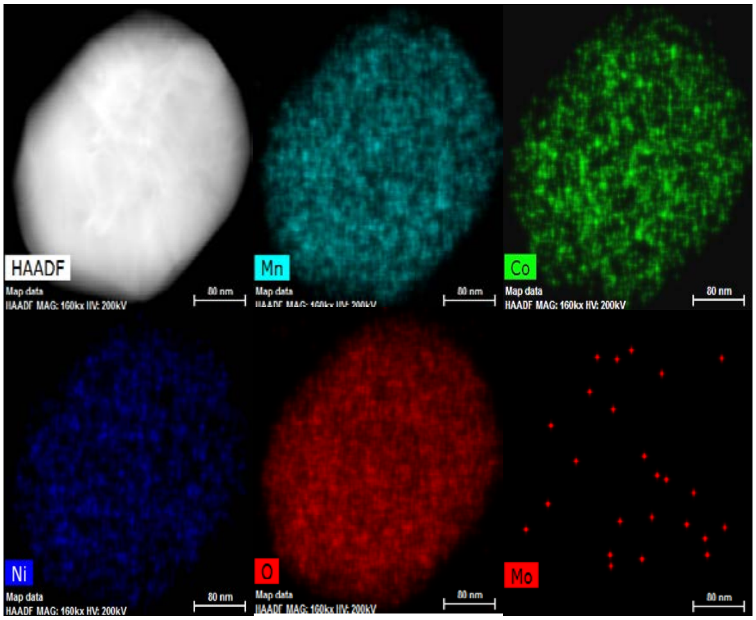

Supplementary Figure 5. EDS mapping of G_4 after water washing

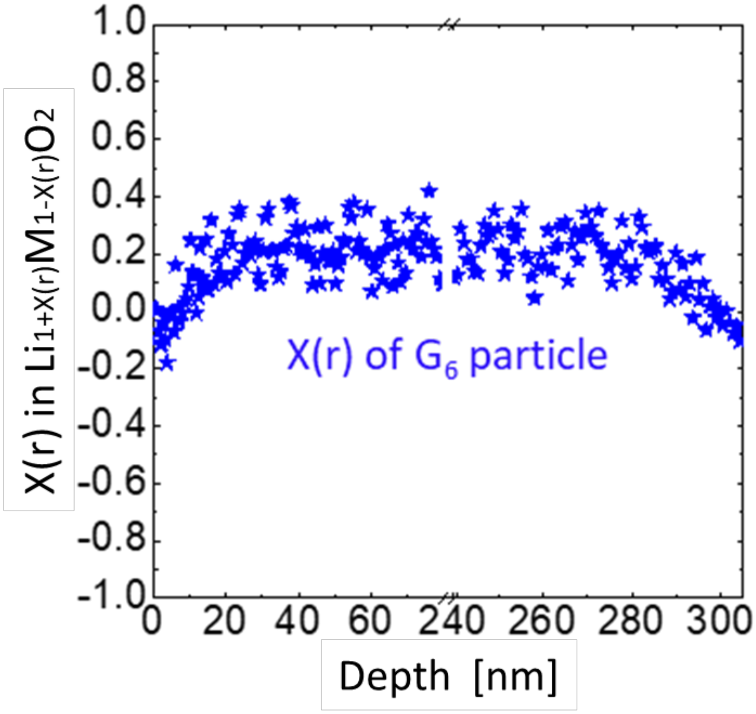

Supplementary Figure 6. The *X*(r) profile from surface to bulk within a G_6 particle

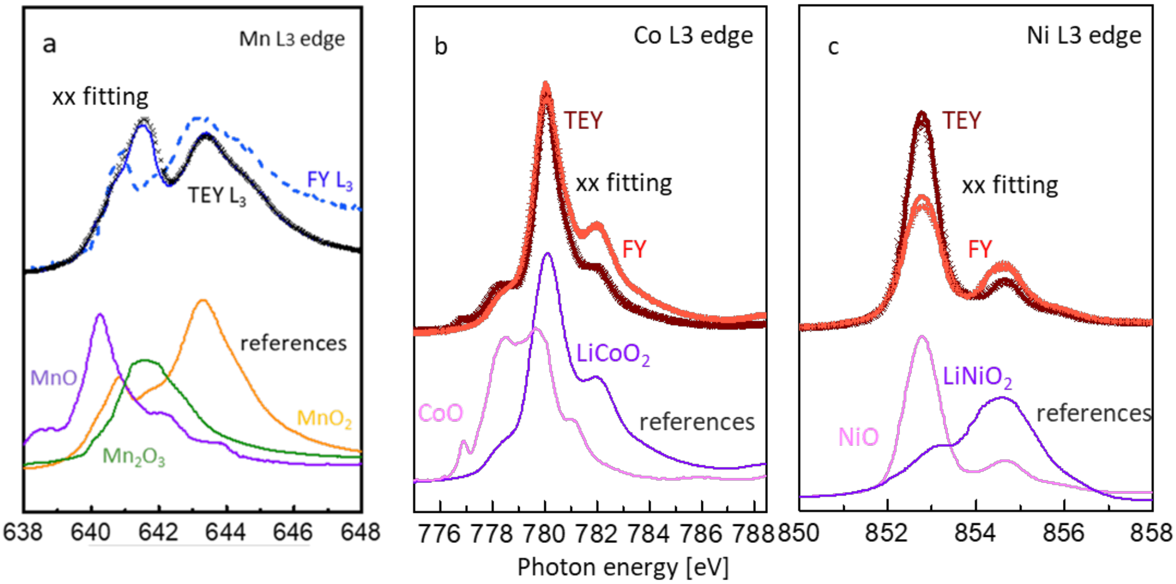

Supplementary Figure 7. sXAS L_3 edge of (a) Mn, (b) Co, (c) Ni in G_4 particles collected from FY and TEY modes with linear fitting by standard references. All the M L_3 edges are quantitatively fitted with linear combination of standard references to indicate the M valence in the bulk and at the surface of G_4 particle. Because of the self-absorption and saturation effects[3], linear fitting is not carried out on Mn FY L_3 edge. The quantitative fitting on Mn TEY L_3 edge shows that 5% Mn^{2+}, 54% Mn^{3+} and 41% Mn^{4+} were contained up to 10 nm depth in the Li-poor surface, and so the average Mn valence is +3.36 at G_4 surface. The linear fitting on Co L_3 edge shows that Co valence is 100% in +3 in the bulk, and comprise of 5% Co^{2+} and 95% Co^{3+} (average valence: +2.95) at the surface. The linear fitting on Ni L_3 edge shows that that Ni ions at the surface are 100% Ni^{2+}, whereas mixture of 61% Ni^{2+} and 39% Ni^{3+} (average valence: +2.39) in the bulk[4-6].

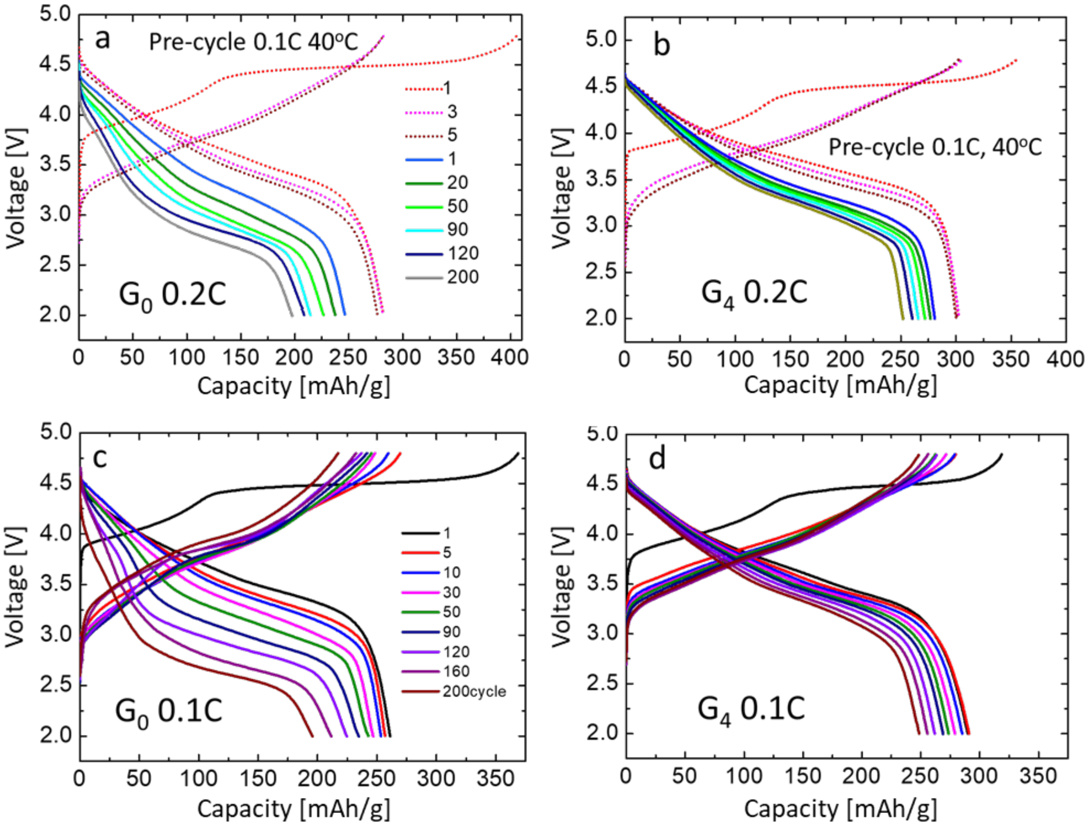

Supplementary Figure 8. Charge/discharge profiles of (a) G_0 and (b) G_4, pre-cycled at 40 °C, 0.1C (dash line) for formation and then cycled at 25 °C, 0.2C. (c-d) Charge/discharge profiles of (c) G_0 and (d) G_4 at 25 °C, 0.1 C.

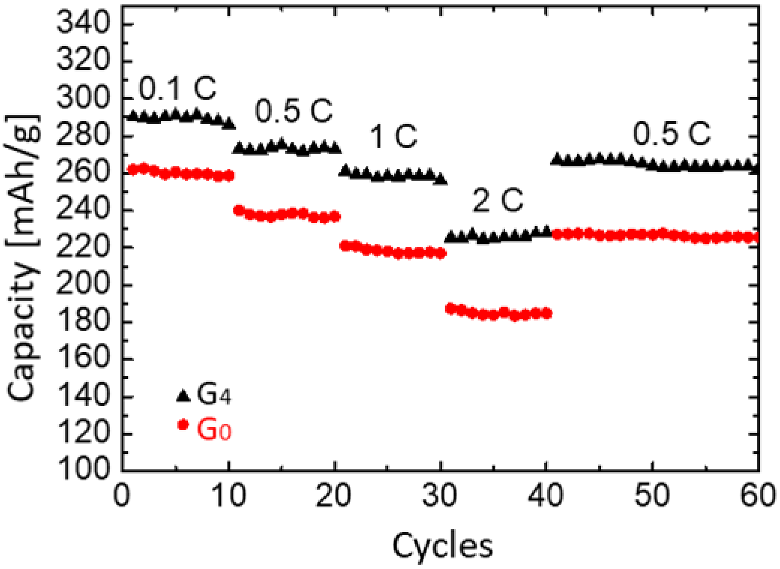

Supplementary Figure 9. Capacity retention of G_0 and G_4 at different rates

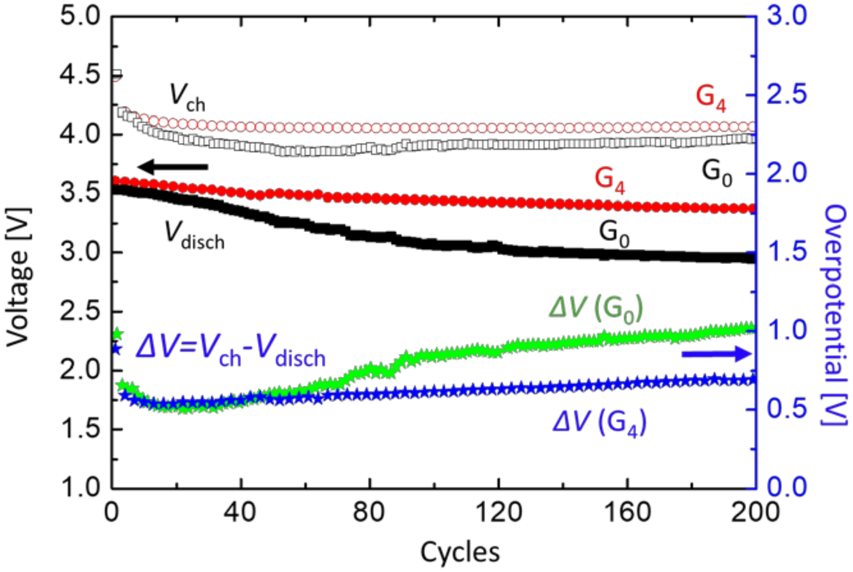

Supplementary Figure 10. The average voltages of cyclic charge/discharge under 0.2C. From the cyclic average charge voltage ($\bar{V}_{ch}$) and discharge voltage ($\bar{V}_{disch}$) between G_0 and G_4 (constant current cycling at 0.2 C), it can be clearly seen that the over-potentials ($\Delta\bar{V} \equiv \bar{V}_{ch} - \bar{V}_{disch}$) between charge and discharge were similar for G_0 and G_4 in the initial 40 cycles, both around 0.54 V. However, $\Delta\bar{V}$ of G_0 increased to >1.02V while that of G_4 only increased to 0.69 V after 200 cycles.

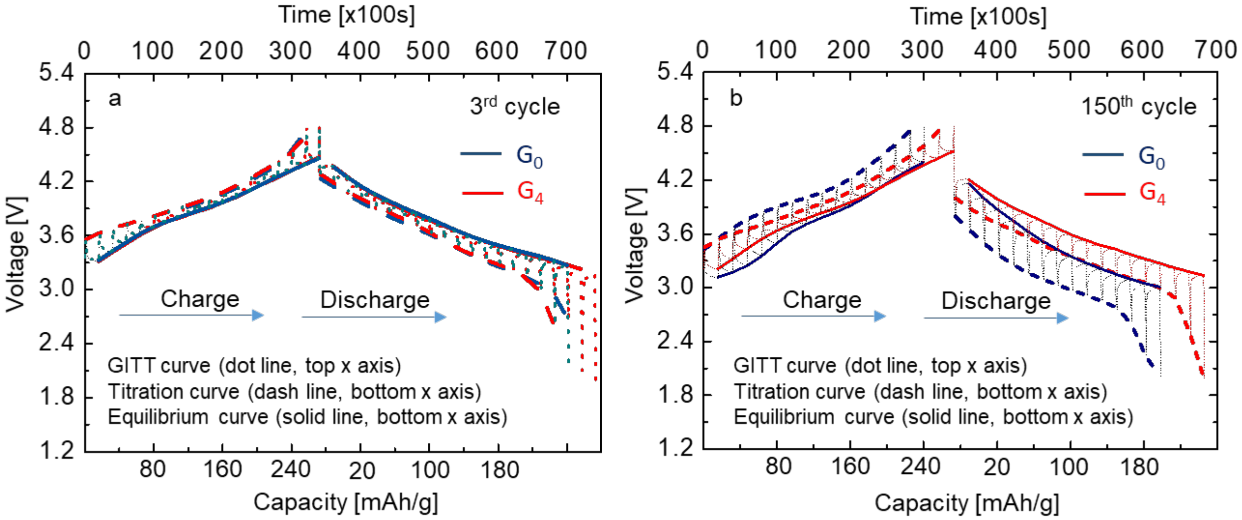

Supplementary Figure 11. GITT curves performed on G_0 and G_4 in the 3rd and 150th cycle

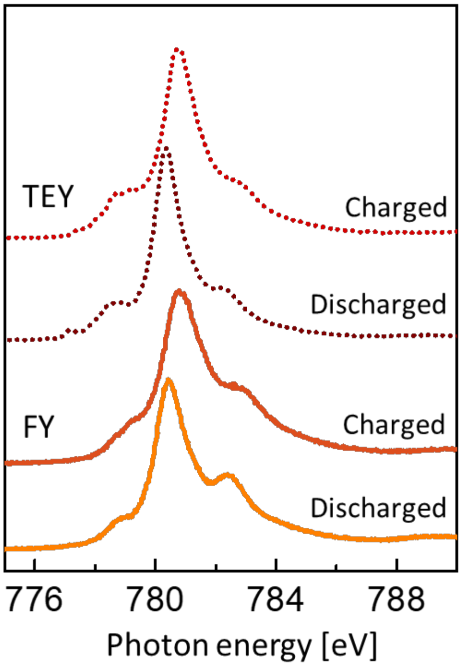

Supplementary Figure 12. Co sXAS L_3 edge in G_4 particle at discharged and charged states

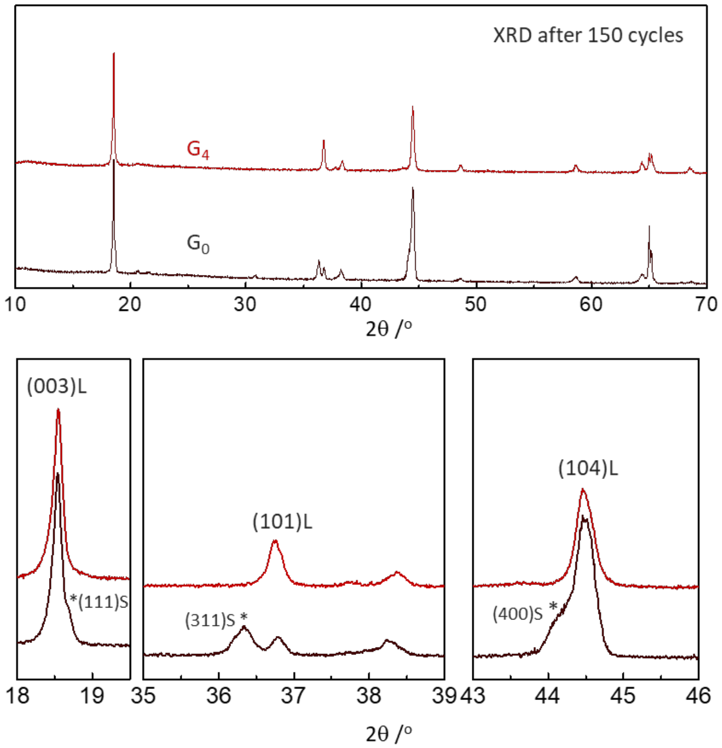

Supplementary Figure 13. XRD patterns of G_0 and G_4 cathodes after 150 cycles. It clearly shows that massive impurities, which can be due to spinel phases (marked with *), was obtained in G_0 cathode after 150 cycles, while those were little on the XRD pattern of G_4. Besides, the peak ratio of $I_{(104)}/I_{(003)}$ increased a lot on G_0, indicating that massive layered phase transformed to disordering or rock salt phase after 150 cycles.

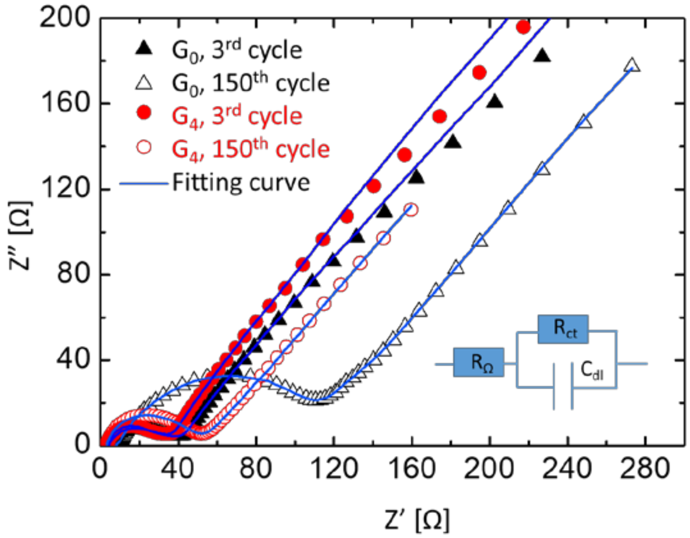

Supplementary Figure 14. EIS curves for G_0 and G_4 in the 3rd and 150th cycle. From the EIS result, it can be clearly seen that R_{ct} of G_0 was 41Ω while that of G_4 was 38Ω in the 3rd cycle, which was quite similar. However, after 150 cycles, R_{ct} of G_0 increased to ~90Ω, while that of G_4 only increased to 52Ω.

Therefore, the R_{ct} for G_4 sample remained stable and the value is much smaller than that of G_0 after 150 cycles. The different R_{ct} between G_0 and G_4 was consistent with the different over-potentials between the two samples after 150 cycles.

Supplementary Table 1 ICP-AES results for the filtered solution. ICP of the washed-away solution of G_4 showed Li:Mo ratio of ~2 and almost no Mn, Ni and Co, which also proved that no M was lost from the particle and the washed product was $LiMoO_4$

Li	Mo	Mn	Ni	Co
2.013	1	<0.001	<0.001	<0.001

Supplementary Table 2 ICP-AES results for G_0 and G_4 samples. The solution were diluted to 30 ug/mL and 20 ug/mL, and measured twice under each solution concentration and for each sample (4 data points for G_0 and G_4 each). Data is normalized to keep the sum of Mn/Co/Ni as constant 0.80 (since no M lost from the particle in Supplementary Table 1). The average content of Li was 1.221 in G_0 sample and 1.173 in G_4, with standard error of ±0.003 and ±0.003, respectively. The errors are calculated as the standard deviations of the four measurements for each sample. ICP of G_4 further indicated that Mo was totally removed after washing in water, as there was no Mo found in G_4.

	G_0				G_4				
	Li	Mn	Ni	Co	Li	Mn	Ni	Co	Mo
30 ug/mL (particle)	1.215	0.478	0.158	0.165	1.165	0.475	0.155	0.166	<0.001
	1.224	0.483	0.156	0.161	1.175	0.479	0.160	0.161	<0.001
20 ug/mL (particle)	1.216	0.476	0.163	0.161	1.172	0.484	0.159	0.159	<0.001
	1.227	0.483	0.157	0.158	1.180	0.481	0.163	0.158	<0.001
Mean	1.221	0.480	0.159	0.161	1.173	0.480	0.159	0.161	<0.001
Standard deviation	**0.003**	0.002	0.002	0.001	**0.003**	0.002	0.002	0.002	

Supplementary Table 3 ICP-AES results for G_0 after water-washing at 70 °C, which will be discussed in Supplementary Discussion 1

	Li	**Mn**	**Ni**	**Co**
30 ug/mL (particle)	1.197	0.484	0.156	0.160
	1.206	0.479	0.162	0.159
20 ug/mL (particle)	1.199	0.480	0.159	0.161
	1.205	0.477	0.158	0.165
Mean	**1.202**	**0.480**	**0.159**	**0.161**

Supplementary note 1

Estimation of electrons extracted in the charge process by sXAS O K edge

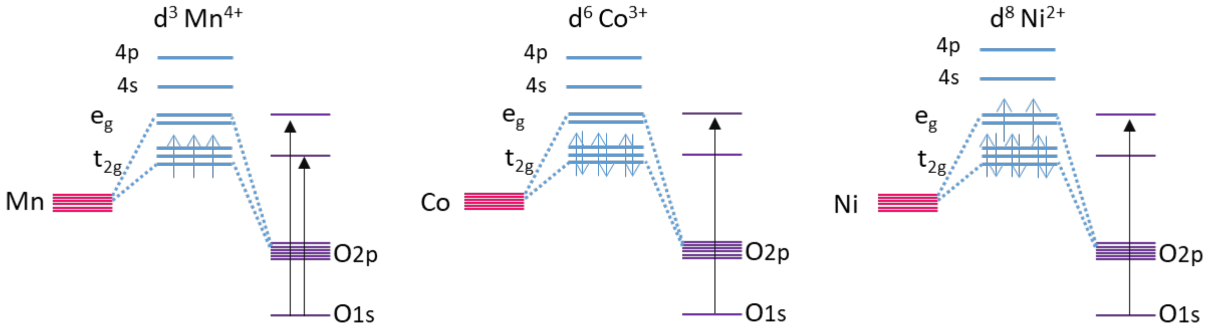

Schematic diagrams of XAS transitions from O1s to the holes on each transition metal[7]

The integral of the O K edge XAS for $Li_{1.20}[Ni^{2.5+}_{0.16}Co^{3+}_{0.16}Mn^{4+}_{0.48}]O_2$ material during charging can be used to indicate the number of electrons removed from both M_{3d} and O_{2p} (holes created) orbitals in the charge process, since $O_{1s}\rightarrow$holes transition probability is proportional to the number of holes on M_{3d} and O_{2p}. Because all M ions are hybridized with O in the material, any electron escaped from M or O can be reflected from the O K-edge. The schematic diagrams above show the hybridized M_{3d} and O_{2p} states, which leads to the O K edge XAS peaks at 530 eV (t_{2g} and up-spin on e_g) and 532 eV (down-spin on e_g). For Mn^{4+}-O, there are 3 holes on t_{2g} and 4 holes on e_g so that there are 7 possible XAS transitions associated with Mn-O, for Co^{3+}-O, there are 4 holes on e_g, and for $Ni^{2.5+}$-O, there are 2.5 average holes on e_g. Thus for $Li_{1.2}[Ni^{2.5+}_{0.16}Co^{3+}_{0.16}Mn^{4+}_{0.48}]O_2$, there can be $4.4(0.48\times7+0.16\times4+0.16\times2.5)$ possible XAS transitions in total from O_{1s}. After charge, electrons from M_{3d} or O_{2p} were removed, so that there can be more holes generated, and resulted in an enlarged O K edge XAS peaks at 530 eV and 532 eV. If the integral of O pre K edge after charged was $a\times$ ($a>1$) that of the discharged states, then the average number of holes (δ^+) in the bulk per formula unit should satisfy $4.4+\delta^+=4.4\times a$. So

$$\delta^+=4.40(a-1)$$

and δ^+ can be the total number of removed electrons from both M and O ions.

Similarly, for the Li-poor $Li_{0.95}Mn_{0.63}Co_{0.21}Ni_{0.21}O_2$ surface, Mn owns 0.63×6.2 holes, Co owns 0.21×4 holes and Ni owns 0.21×2 holes, so the overall number of holes from the Li-poor surface can be estimated by

$$\delta^+=5.15(a-1).$$

From Fig. 4a, the integration of O K edge sXAS peaks at 527.5 eV-534.2 eV after charge collected at FY mode is $a=1.238$ times that of the discharged states, so we can calculate **δ^+= ~1.05** (329 mAh/g) from the Li-rich bulk, which is very close to the actual charged 323 mAh/g in the first cycle. However, based on the integral change of O K edge XAS peaks at TEY mode ($a=1.157$), only **δ^+= ~0.81** (221 mAh/g) is obtained from the Li-poor surface.

Supplementary Discussion 1

Analysis and consistency between the amount of used MoO_3, generated Li_2MoO_4 and leached Li from Li gradient region

From the ICP result in Supplementary Table 2, we obtain the overall composition of G_0 to be $Li_{1.221}Mn_{0.48}Co_{0.16}Ni_{0.16}O_2$. However, we also analyzed the component of G_0 after water washing at 70 ^oC to remove the possible Li_2CO_3 or LiOH, and obtained a Li composition of 1.202 (Supplementary Table 3). Therefore, the 1.221-1.202=0.019 excess Li should come from the unreacted Li_2CO_3 or LiOH in the initial G_0 sample, which can be removed after water-washing.

The ICP result indicates that Mn, Co, Ni content was not lost in the leaching process, while the Li content was reduced to 1.173 in Supplementary Table 1-2. The decreased **ΔLi=-0.048** (1.173-1.221) was exactly double the amount of MoO_3 used (0.0238, 4 wt%, also see Supplementary Table 2). Therefore, all MoO_3 has transformed to Li_2MoO_4 after leaching and the amount was 0.0238. The composition is thus 1 $Li_{1.173}Mn_{0.48}Co_{0.16}Ni_{0.16}O_{1.973}$ (M=85.0) + 0.238 Li_2MoO_4, so Li_2MoO_4 is calculated to be **4.7wt%** (0.0238 ×174/(0.0238×174+85.0)) in the intermediate product. After washing with water, this Li_2MoO_4 layer is totally removed, as seen in Supplementary Fig. 5. The weight loss after water washing was carefully measured to be **4.9±0.1%**, which is very close to the ICP analysis.

Furthermore, ICP is consistent with EELS line scan results. From the ICP of G_0, we note that ΔLi= -0.029 (1.173-1.202) was leached from the Li-rich particle, while 0.019 Li was from the Li_2CO_3 or LiOH. Meanwhile, EELS line scan across the G_4 particle in Fig. 3 indicates that the bulk composition is still $Li_{1.20}Mn_{0.48}Co_{0.16}Ni_{0.16}O_2$ (X(bulk)=0.2), and in the Li gradient region (with $X(r)$ gradually decreasing from 0.20 to ~-0.05) is ~17 nm thick on a ~400 nm diameter particle surface, and so the volume of the gradient region can be estimated as ~23.4% of the whole particle. Assuming that $X(r)$ changes linearly from 0.2 in the bulk to -0.05 at the surface, we can estimate that ΔLi =~**-0.0293** (=0.234×(-0.05-0.20) ×1/2) is lost in this gradient region, very close to the Li amount (-0.029) that was leached by MoO_3 from the G_0 particle (excluding the Li from Li_2CO_3 or LiOH). Therefore, we can infer that almost all the leached LiO by MoO_3 from G_0 was leached from the ~17 nm thick Li gradient region on G_4 surface.

Supplementary Discussion 2

The voltage (V) in "voltage fade" consists of two parts $V = V^{OCV} + V^{P}$, where the open-circuit V^{OCV} is thermodynamic, and the overpotential V^{P} is kinetic polarization which depends on the direction and magnitude of the current. Both V^{OCV} and V^{P} can change with cycle number n, reflecting change in the composition and kinetic resistance, respectively. So the voltage fade with cycling will have contributions from both ΔV^{OCV} and ΔV^{P}. From the GITT analysis in Supplementary Fig. 11, where the solid line is V^{OCV} and the dash line is $V^{OCV} + V^{P}$ (the difference is the kinetic polarization at any given state of charge/discharge), we can clearly see that at any given state of discharge, say 180 mAh/g, G_4's V^{OCV} and V^{P} both changed very little at 150th cycle (right) compared to 3rd cycle (left). This is because G_4 is both chemically and structurally very stable. However, G_0's V^{P} clearly enlarged by more than factor of 3 at 180mAh/g discharge, indicating greatly increased kinetic impedance, matching with the structural collapse seen at its surface in Fig. 5. Furthermore, G_0's V^{OCV} also drooped down significantly (thanks to referee's excellent insight): whereas there was essentially no difference between $V^{OCV}(G_0)$ and $V^{OCV}(G_4)$ at 3rd cycle, by 150th cycle $V^{OCV}(G_0)$ has dropped significantly at 180mAh/g, indicating permanent change in its chemistry. The thermodynamic OCV change and kinetic polarization change account for roughly

25% : 75% of the "voltage fade" at 180mAh/g discharge in this GITT experiment. We want to mention that this ratio depends on the current density as well as the state of charge/discharge.

Supplementary Discussion 3

Estimation of the capacity contributions of each element in the charge process

From the FY (bulk) sXAS of Mn in Fig 4, it can be seen that there is no obvious change of Mn valence from discharged to charged state, both being Mn^{4+}, so Mn ions contributed no capacity in the charge process in the bulk. Co was also oxidized in the charging process in G_4 particles, according to the changes of Co XAS L_3 edge[8] in Supplementary Fig. 12. And since we do not have reference sample of Co^{4+}, we cannot precisely determine the voltage at which $Co^{3+} \rightarrow Co^{4+}$, but we can estimate that it can *at most* contribute 0.16×(4-3.0)=0.16 e in the bulk (FY). Also, Ni ions can be estimated as +4 valence at most after charge. As Ni ions before charge was +2.39 (Supplementary Fig. 7) in the $Li_{1.2}Mn_{0.48}Co_{0.16}Ni_{0.16}O_2$ bulk, so Ni ions can donate 0.16× (4-2.4) =0.26 e at most in the charge process. Thus, in the Li-rich bulk, M can at most contribute 0.42 e (26801*(0.26+0.16)/MW=132 mAh/g, where MW=85.5). As discussed in Supplementary note 1, 1.05 e has been charged from the $Li_{1.2}Mn_{0.48}Co_{0.16}Ni_{0.16}O_2$ bulk, and so we can infer that oxygen had contributed at least 1.05-0.26-0.16 =**0.63 e** (26801*0.63/MW=197 mAh/g) in the charge process. Please note, as the Li poor surface also contributes to FY sXAS, the capacity contribution here actually comprises of a majority from the Li-rich bulk and a minor from the Li-poor surface. Theoretically, M in the pure Li-rich bulk can only contribute 0.16×(4-3)+0.16×(4-2.5)=0.40 e (125 mAh/g) at most, while the rest 0.65 e (204 mAh/g) comes from the oxygen anion redox as shown in Fig. 1a and Fig. 4h.

For the surface of $Li_{0.95}Mn_{0.63}Co_{0.21}Ni_{0.21}O_2$ (MW=97.9), however, according to the TEY data in Fig. 4, we can see that Mn ions in the discharged state is +3.36, but changes to +3.96 after charge, and so Mn contributed 0.63×(3.96-3.36) =0.38 e. Assuming all the 0.81e are all from M redox, and the average valence of Ni and Co is +2.5 (Supplementary Fig. 7) before charging, then the average valence of Co and Ni can be oxidized to (0.81-0.38)/0.42+2.5=3.52. This value is far below of the +4 valence that Co and Ni can be oxidized to in LMO material before activating the oxygen redox.

Supplementary discussion 4

Galvanostatic Intermittent Titration Technique (GITT) is performed on G_0 and G_4 in the 3rd cycle and 100th cycle, as shown in Supplementary Fig. 11. Li diffusivity in Fig. 6 is calculated by:

$$D_{Li} = 4/\pi\tau \times (\Delta E_s/\Delta E_t)^2 L^2$$

Here, τ is the duration of the current pulse (200s); ΔE_s is the steady-state voltage change due to the current pulse, ΔE_t is the voltage change during the constant current pulse, and L is the Li ion diffusion distance. In this measurement, we assume that the Li diffusion is the limiting step, and so iR drop is excluded. L is taken as the radius of primary particle. Though the value of L is hard to measure and can affect D_{Li} by a lot, all D_{Li} values are calculated with the same particle size before and after cycles. The trend of D_{Li} change in cycling can directly reflect the impedance change between G_0 and G_4.

From GITT analysis we obtained the average Li^+ diffusivity (D_{Li}) in the lattice of G_0 and G_4 in the 3rd and 150th cycle. We found that the D_{Li} of G_0 and G_4 were also similar in the 3rd cycle, but after 150 cycles, the two samples have significantly different D_{Li}. The results are added in Fig. 6a. In the charge process,

G_4 has similar D_{Li} with G_0 in the 3rd cycle, both (3~6)×10^{-12} cm^2/s. However, after 150 cycles, the D_{Li} of G_0 decreased to (2~6)×10^{-13} cm^2/s while that of G_4 still keeps (1~5)×10^{-12} cm^2/s.

Supplementary References

1 Moser, M., Klimm, D., Ganschow, S., Kwasniewskj, A. & Jacobs, K. Re-determination of the pseudobinary system Li2O-MoO3. *Cryst Res Technol* **43**, 350-354, doi:10.1002/crat.200711106 (2008).

2 Liebertz, J. & Rooymans, C. Phase behaviour of Li2MoO4 at high pressures and temperatures. *Solid State Communications* **5**, 405-409 (1967).

3 Asakura, D. *et al.* Material/element-dependent fluorescence-yield modes on soft X-ray absorption spectroscopy of cathode materials for Li-ion batteries. *AIP Advances* **6**, 035105 (2016).

4 Qiao, R. M. *et al.* Direct evidence of gradient Mn(II) evolution at charged states in LiNi0.5Mn1.5O4 electrodes with capacity fading. *J Power Sources* **273**, 1120-1126, doi:10.1016/j.jpowsour.2014.10.013 (2015).

5 Li, Q. H. *et al.* Quantitative probe of the transition metal redox in battery electrodes through soft x-ray absorption spectroscopy. *J Phys D Appl Phys* **49**, doi:Artn 413003
10.1088/0022-3727/49/41/413003 (2016).

6 Tian, C. X. *et al.* Depth-Dependent Redox Behavior of LiNi0.6Mn0.2Co0.2O2. *J Electrochem Soc* **165**, A696-A704, doi:10.1149/2.1021803jes (2018).

7 Luo, K. *et al.* Charge-compensation in 3d-transition-metal-oxide intercalation cathodes through the generation of localized electron holes on oxygen. *Nat Chem* **8**, 684-691, doi:10.1038/Nchem.2471 (2016).

8 Yoon, W. S. *et al.* Oxygen contribution on Li-ion intercalation-deintercalation in LiAlyCo1-yO2 investigated by O K-edge and Co L-edge X-ray absorption spectroscopy. *J Electrochem Soc* **149**, A1305-A1309, doi:10.1149/1.1503074 (2002).